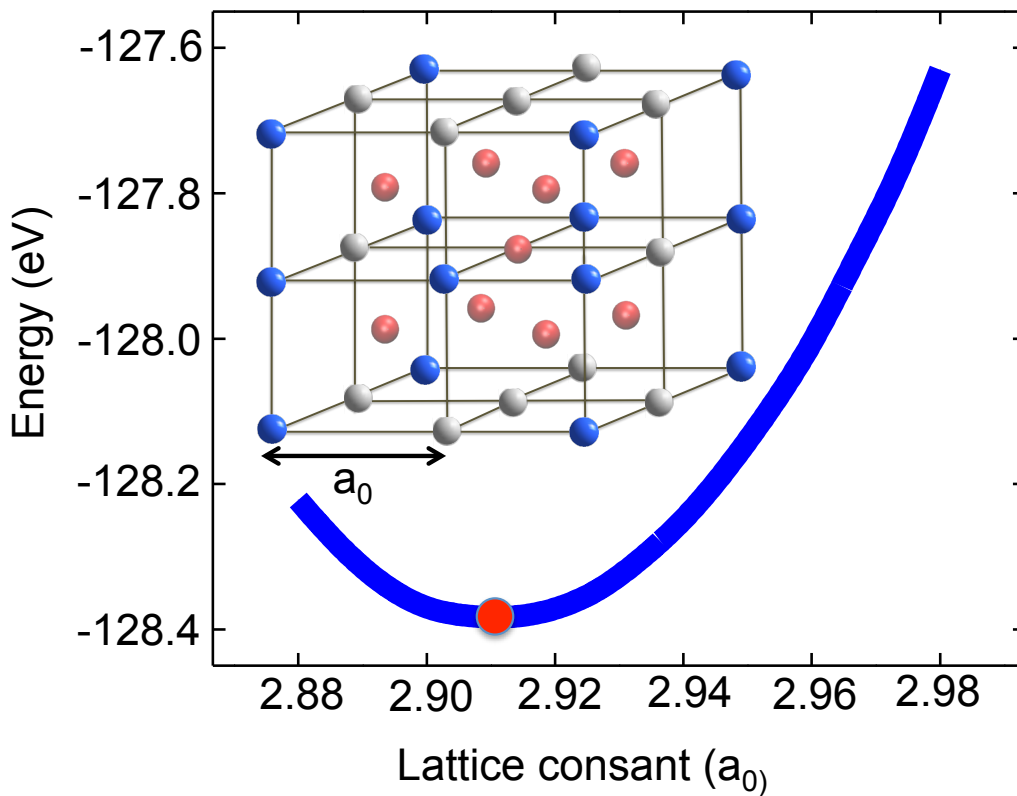


1

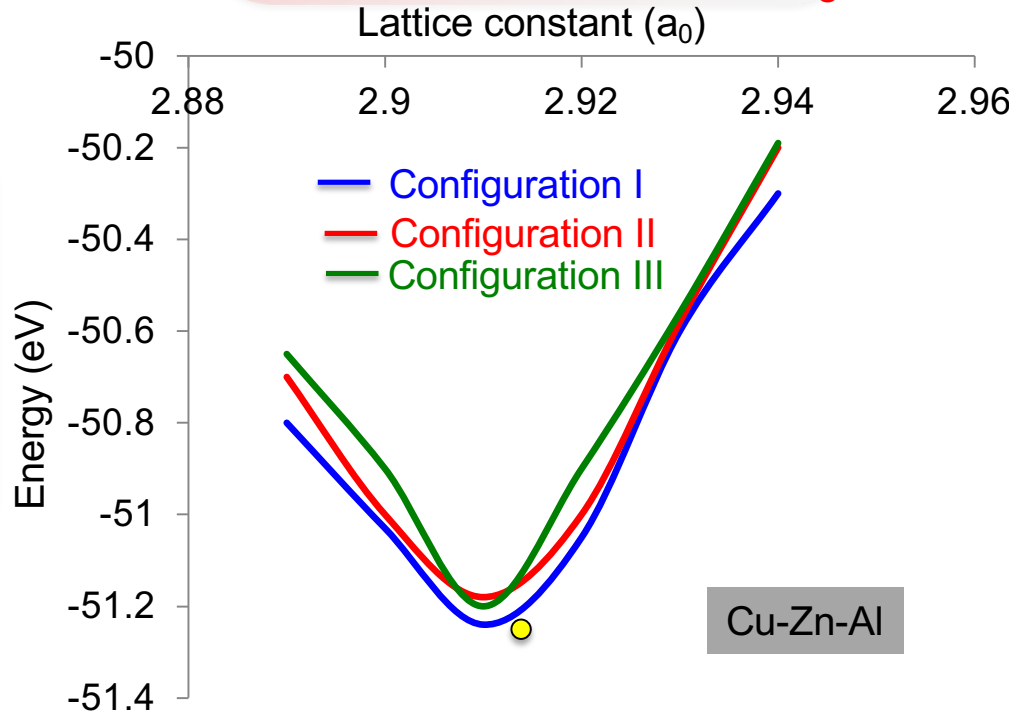
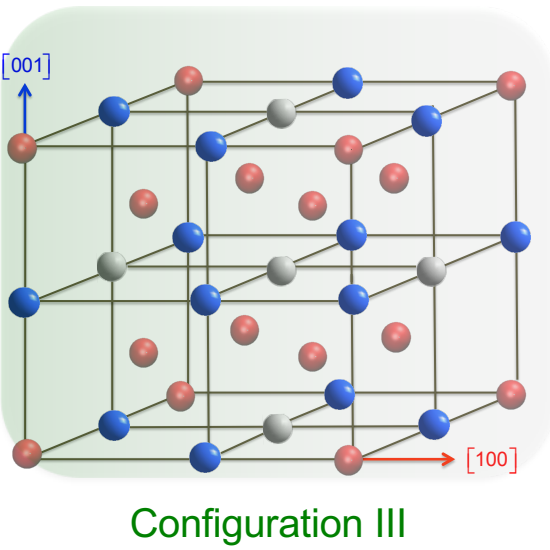
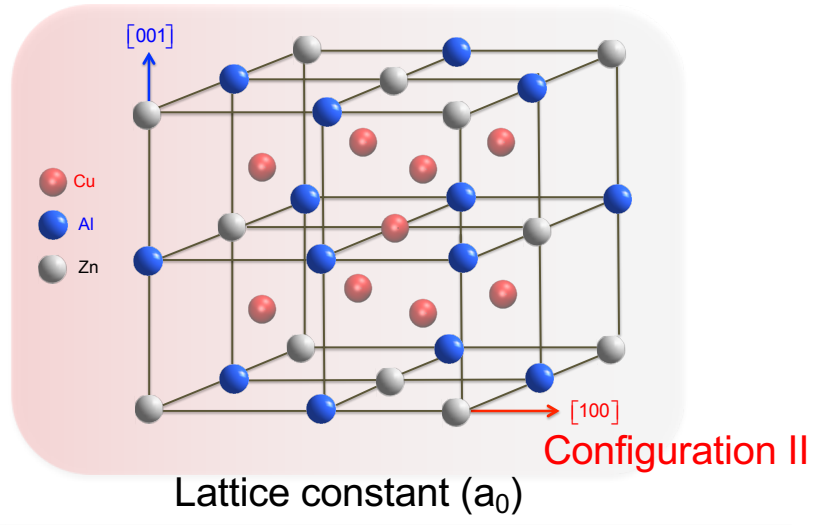
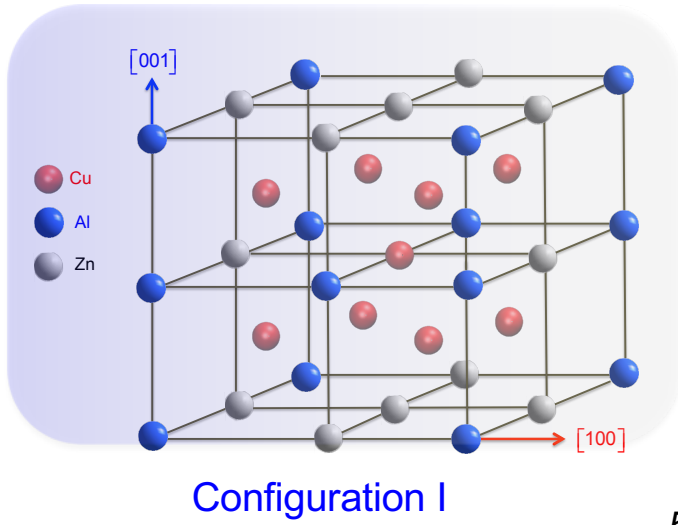
# ME 531- Lecture 8- Further Illustration of the PN Model for Complex BCC type Crystal Lattices

## Energetics of Configuration I

### Lattice constant determination



**Note:** Energy as a function of lattice constant should be obtained for each configuration. The minimum energy values should be noted to obtain the most favorable configuration.



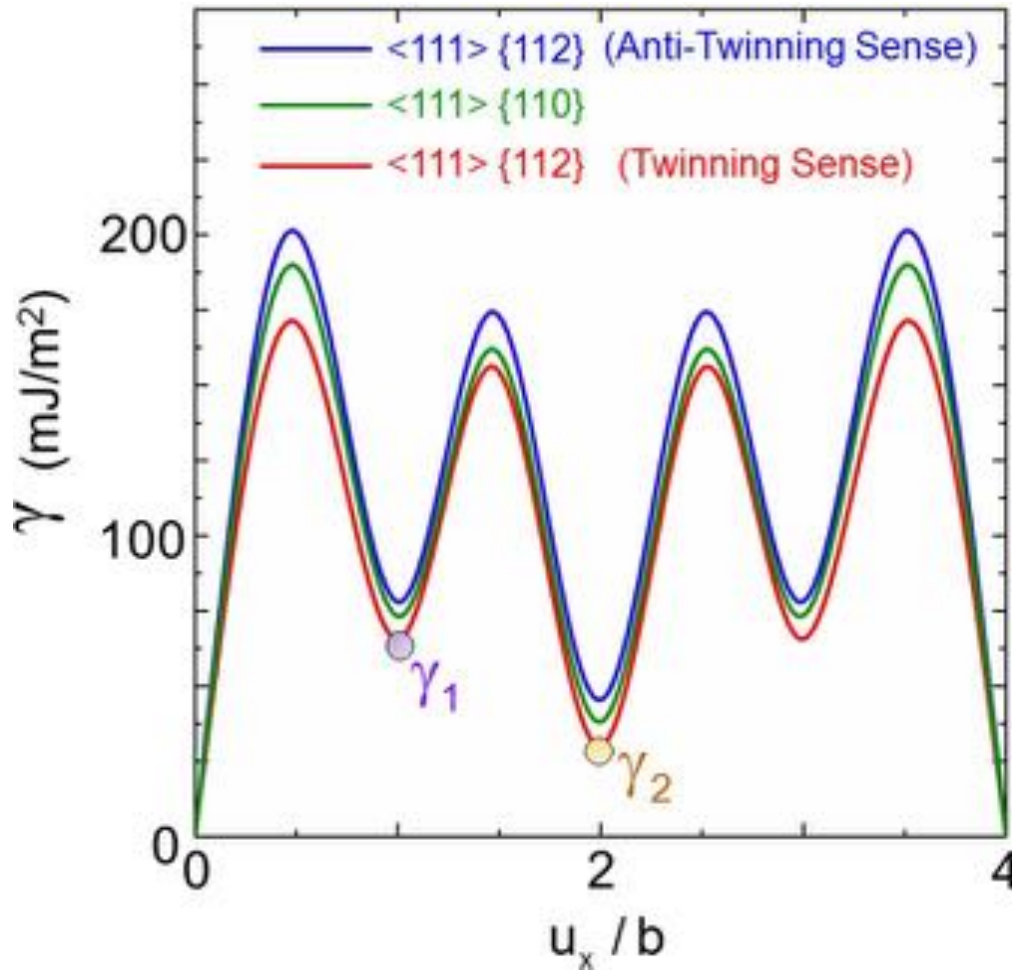


**Figure 1** shows the generalized stacking fault energy (GSFE) curves along  $\langle 111 \rangle \{110\}$  and  $\langle 111 \rangle \{112\}$  slip systems considering the intrinsic asymmetry along the twinning and anti-twinning directions. The disregistry displacement  $u_x$  varies between 0 to a  $\langle 111 \rangle$ . The local minima  $\gamma_1$  and  $\gamma_2$  show the stable NNAPB and NNNAPB fault energy levels.

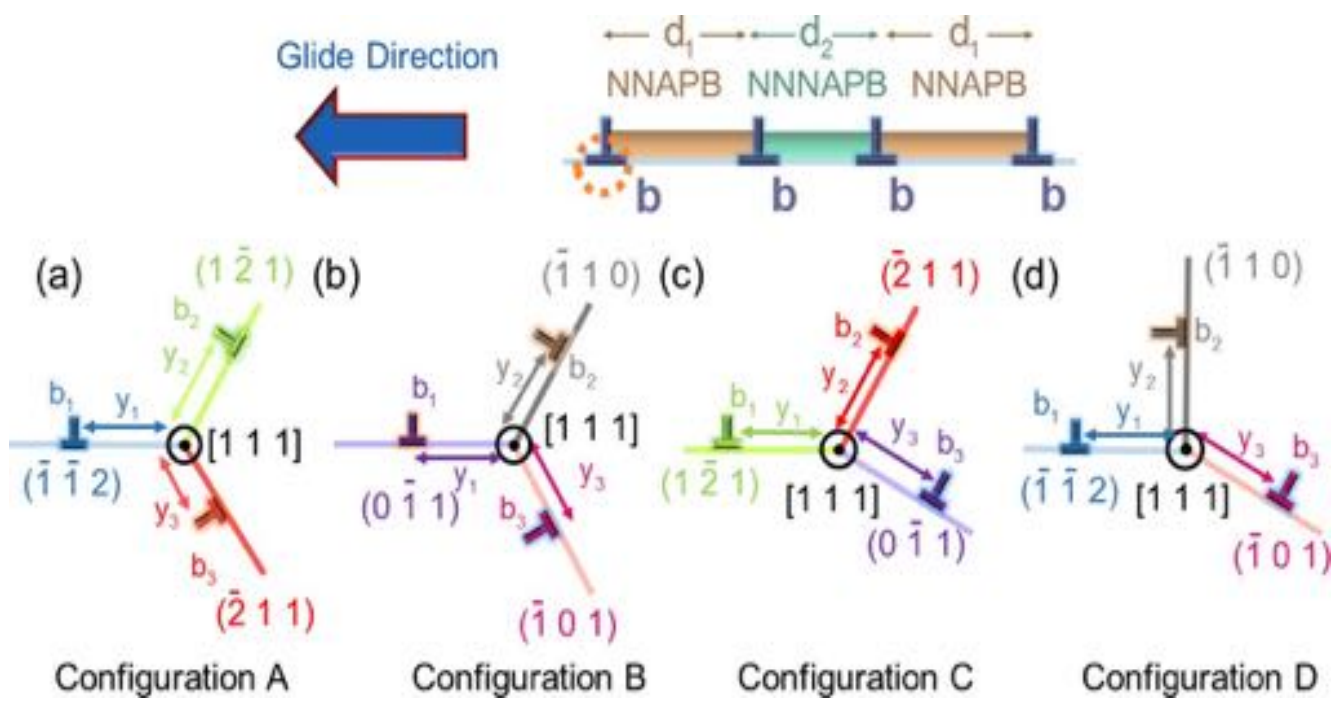


Figure 2 shows the possible core configurations of the  $a/4 \langle 111 \rangle$  leading partial in CuZnAl.

The equilibrium separation distances  $d_1$  and  $d_2$  between the screw partials in externally stress free configuration, as illustrated in Figure 2, are evaluated by the balance of the repulsive dislocation interaction forces with the restoring forces originating from the NNAPB and NNNAPB faults. The stable APB energy values of  $\gamma_1$  and  $\gamma_2$  are related to the distances of  $d_1$  and  $d_2$  as [38]:

$$\gamma_1 = \frac{K_s b^2}{2\pi} \left\{ \frac{1}{d_1} + \frac{1}{d_1 + d_2} + \frac{1}{2d_1 + d_2} \right\} \quad (1)$$

$$\gamma_2 = \frac{K_s b^2}{2\pi} \left\{ \frac{2}{d_1 + d_2} + \frac{1}{2d_1 + d_2} + \frac{1}{d_2} \right\} \quad (2)$$

The resulting  $d_1$  and  $d_2$  values from the simultaneous solution of the expressions in Eq.(1) and (2) are tabulated in Table 1 for both {110} and {112} planes. The explicit calculation of the anisotropic coefficient  $\kappa_s$  is detailed in Appendix A. The resulting value of  $d_1$  is in close agreement with the experimental measurement of 3 nm [27] justifying the GSFE profile in Figure 1 generated from the *ab-initio* calculations.

NNAPB	$\gamma_1$	<111> {112} Twinning Sense	(mJ/m <sup>2</sup> )	61
NNAPB	$\gamma_2$	<111> {112} Twinning Sense	(mJ/m <sup>2</sup> )	26
NNAPB	$\gamma_1$	<111> {112} Anti-Twinning Sense	(mJ/m <sup>2</sup> )	77
NNAPB	$\gamma_2$	<111> {112} Anti-Twinning Sense	(mJ/m <sup>2</sup> )	35
NNAPB	$\gamma_1$	<111> {110}	(mJ/m <sup>2</sup> )	70
NNAPB	$\gamma_2$	<111> {110}	(mJ/m <sup>2</sup> )	31
		$d_1$ {110} (nm)		2.6
		$d_2$ {110} (nm)		13.40
		$d_1$ {112} (nm) (average)		2.7
		$d_2$ {112} (nm) (average)		13.45

**Table 1** tabulates the NNAPB and NNNAPB energy values, i.e.  $\gamma_1$  and  $\gamma_2$ , respectively, extracted from the GSFE curves of <111> {112} slip system along the twinning and the anti-twinning directions and <111> {110} system. The separation distances between the partials under zero external stress, i.e.  $d_1$  and  $d_2$ , are also included. It is to be noted that  $d_1$  and  $d_2$  values on {112} plane are calculated based on the average  $\gamma_1$  and  $\gamma_2$  values of the twinning and the anti-twinning directions.

Among the core configurations illustrated in Figure 2, configuration A favors the core spreading on the conjugate  $\{112\}$  family planes in the  $\langle 111 \rangle$  glide zone. Two (one) of these conjugate planes promote glide in twinning (anti-twinning) sense. In configuration B, the core structure is spread on the conjugate  $\{110\}$  planes. The other possible configurations C and D, consist of a core which spreads on a combination of  $\{112\}$  and  $\{110\}$  planes. At this point, it is important to emphasize that the glide resistance in twinning sense on  $\langle 111 \rangle$   $\{112\}$  system is intrinsically lower than the anti-twinning sense. The departure from symmetry in the glide resistance along  $\langle 111 \rangle$   $\{112\}$  system originates from the symmetry group of bcc-based structures and is also reflected in the GSFE curves generated in Figure 1.

Inside the core of each superpartial, the net  $a/4 \langle 111 \rangle$  Burgers vector is distributed as of disregistry displacements, parallel to  $\langle 111 \rangle$ , on the conjugate  $\{110\}$  and/or  $\{112\}$  planes [12]. An example of the non-planar core disregistry distributions, denoted as  $1(j)=1,2,3$ , for configuration A of Figure 2 (a) is illustrated in Figure 3 (a). It should be noted that the resultant of these slip distributions on the three conjugate planes sum up to  $b$  at the dislocation line center which

Determination of the theoretical CRSS levels requires to incorporate the slip geometry into the total energy expression,  $E_{\text{tot}}$ . This formulation incorporates both long-range elastic and short-range misfit energy terms as well as the work done by the external stress components on the dissociated a <111> dislocation configuration. To that end, the external stress tensor  $\sigma$  applied on the sample should be described with respect to the dislocation coordinate frame. This task is accomplished by transforming the  $\sigma$  tensor from the sample frame  $x_1 - x_2 - x_3$  to the dislocation frame  $x_1 - x_2 - x_3$ . The base vectors of these two orthonormal coordinate systems are denoted as  $\mathbf{E}_1, \mathbf{E}_2, \mathbf{E}_3$  and  $\mathbf{e}_1, \mathbf{e}_2, \mathbf{e}_3$  respectively. As illustrated in Figure 4, these vectors are chosen on purpose in both coordinate frames. Meanwhile,  $\mathbf{E}_2$  coincides with the outwards normal of the surface on which the uniaxial loading is applied; the vectors  $\mathbf{e}_2$  and  $\mathbf{e}_3$  are chosen to be parallel to the active glide plane normal and its Burgers vector respectively. The transformation of the coordinates from the sample to the dislocation frame is accomplished via the orthogonal matrix  $\mathbf{Q}_{ij}$  which is described as  $\mathbf{Q}_{ij} = \mathbf{e}_i \cdot \mathbf{E}_j$  where  $i, j = 1, 2, 3$  (  $\cdot$  ) is the dot product operator). Following the second order tensor transformation rules, the external stress tensor is transformed to the dislocation coordinate frame,  $\Sigma_i$ , as in Eq.(1) where the summation convention is implied.

$$\Sigma_i = \mathbf{Q}_k \mathbf{Q}_{jm} \sigma_{km} \quad (i, j, k, m = 1, 2, 3) \quad (3)$$

Similarly, the transformation of the coordinates from the cubic crystal coordinate frame to the sample frame is accomplished by the orthogonal matrix  $\mathbf{R}$  and its components are defined as  $\mathbf{R}_i = \lambda_i \cdot \mathbf{E}_j$  where  $\lambda_i$  are the unit base vectors of cubic crystal frame in Figure 4.

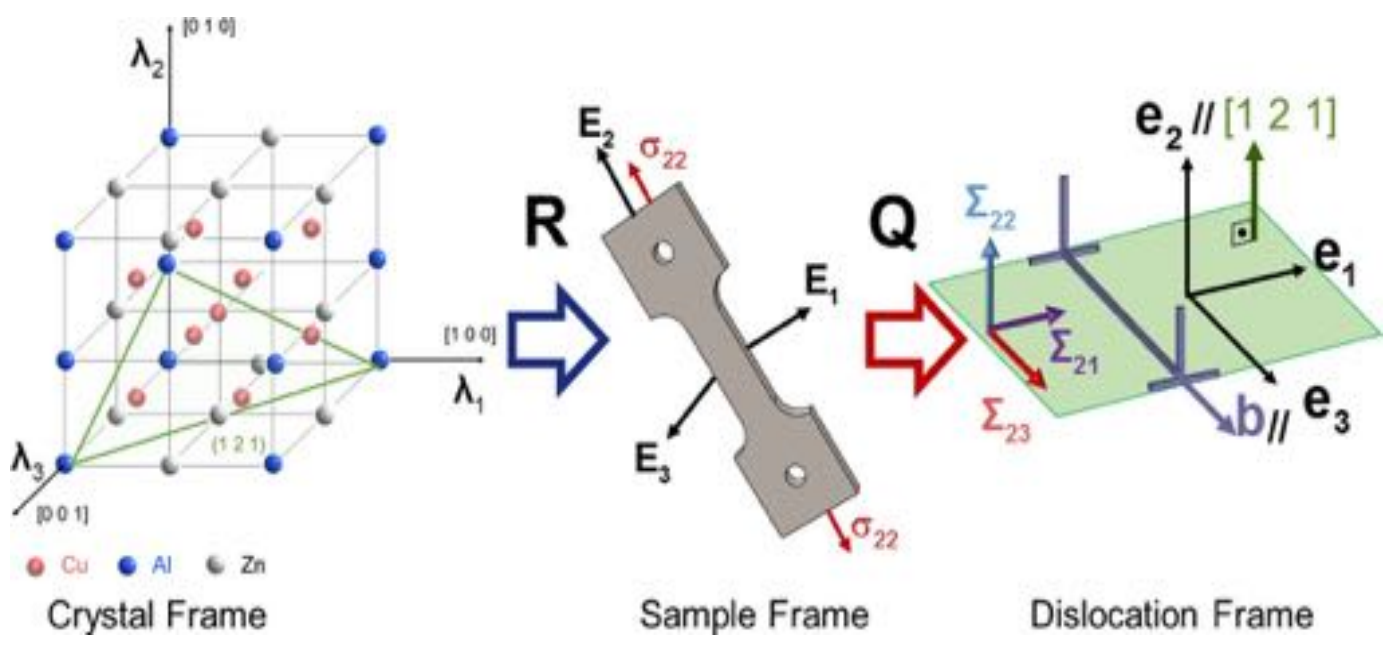


**Figure 4** illustrates the cubic crystal frame  $[100]$ - $[010]$ - $[001]$ , sample frame i.e.  $x_1 \rightarrow x_2 \rightarrow x_3$  (with the base vectors of  $E_1 \rightarrow E_2 \rightarrow E_3$ ) and the dislocation frame i.e.  $x_1 \rightarrow x_2 \rightarrow x_3$  (with the base vectors of  $e_1 \rightarrow e_2 \rightarrow e_3$ ). As can be seen, the coordinate transformation matrices  $R$  and  $Q$  can be used to transform the corresponding coordinates between the cubic, the sample and the dislocation frames.

In order to establish a solution scheme,  $E_{tot}$  is constructed explicitly as the equilibrium of the system corresponds to the minimum total energy configuration, i.e.  $\min.(E_{tot})$ , whether an external stress field is present or not. Following this step, we delineated an energy minimization algorithm to find the updated positions of the leading partial- core fractionals under increasing loading intensity. In this proposed scheme, CRSS level corresponds to the glide shear stress, i.e.  $\Sigma_{23}$ , beyond which the matrix of second order partial derivatives (Hessian matrix) of  $E_{tot}$  function has no positive eigenvalues with the prescribed constraint of positive fractional Burgers vectors.  $E_{tot}$  is composed of: (i) the individual line energies of the four partials:  $E_{line}$ , (ii) the interaction of the long-range elastic fields of these four partials:  $E_{int}$ , (iii) the misfit energies introduced due to the presence of NNAPB and NNNAPB faults:  $E_{mis}$  and (iv) the work done by the external stress field  $W$ .

$$E_{tot} = E_{line} + E_{int} + E_{mis} - W \quad (4)$$

The  $E_{line}$  term can be expressed as the sum of the individual line energies of four  $a/4$   $\langle 111 \rangle$  partials as follows:

$$E_{line} = E_{line,1} + E_{line,2} + E_{line,3} + E_{line,4} = E_{line,1} + 3 \frac{K_3 b^2}{4\pi} \ln \left( \frac{R}{\xi} \right) \quad (5)$$

The variables  $R$  and  $\xi$  represent the outer cut-off and inner-cut off distances which are chosen as  $500 b$  and half of the interplanar spacing,  $a'$ , across  $\langle 111 \rangle$  direction-complying with the original Peierls-Nabarro analysis [47]- respectively. The slip initiation along  $\langle 111 \rangle$   $\{110\}$  or  $\langle 111 \rangle$   $\{112\}$  systems is associated with the glide of the leading partial; therefore, its individual line

energy,  $E_{\text{line},1}$ , is detailed in a fashion including the short-range energy contribution of the fractional dislocations composing the leading partial dislocation.

The long range interaction energy of the  $a/4$   $\langle 111 \rangle$  partials with each other,  $E_{\text{int}}$ , is expressed in Eq.(6) where  $p$  represents the number of the total partials, i.e. 4, and the separation distance between the third and fourth partials (the leading partial is denoted as the first partial), i.e.  $d_3$ , is taken as equal to  $d_1$  as shown in Figure 2 [48, 49]:

$$E_{\text{int}} = \frac{K_s b^2}{4\pi} \left\{ \sum_{i=1}^{p-1} \left[ \sum_{j=1}^i \ln \left( \frac{R}{d_j} \right) + \sum_{j=2}^i \ln \left( \frac{R}{d_j} \right) + \sum_{j=3}^i \ln \left( \frac{R}{d_j} \right) \right] \right\} \quad (6)$$

The misfit energy created on the glide plane via creating stable NNAPB and NNNAPB fault ribbons spanning  $d_1$  and  $d_2$  distances in the dissociated configuration of a  $\langle 111 \rangle$  dislocation,  $E_{\text{mis}}$  is formulated as (2NNAPB and 1 NNNAPB type faults):

$$E_{\text{mis}} = 2\gamma_1 d_1 + \gamma_2 d_2 \quad (7)$$

Lastly, the energy contribution of the work done by the external stress,  $W$ , on the leading partial dislocation configuration is expressed in Eq.(10) as:

$$W = b_1 \tau_1 + b_2 \tau_2 + b_3 \tau_3 \quad (8)$$

where  $\{\tau_1, \tau_2, \tau_3\} = \{\Sigma_{23}, \Sigma_{23} \cos \omega - \Sigma_{13} \sin \omega, \Sigma_{23} \cos \alpha + \Sigma_{13} \sin \alpha\}$  following the coordinate transformation operations. It should be emphasized that as the CRSS level is determined based on the glide motion of the leading partial; the trailing partials do not contribute to the work expression in Eq.(8). The resolved components  $\{\tau_1, \tau_2, \tau_3\}$  are illustrated in Figure 5 along with the non-planar structure of the leading partial core. It is to be noted that the conjugate plane angles,  $\alpha$  and  $\omega$ , are determined based on the geometry of the possible four core configurations A, B, C and D shown in Figure 2.

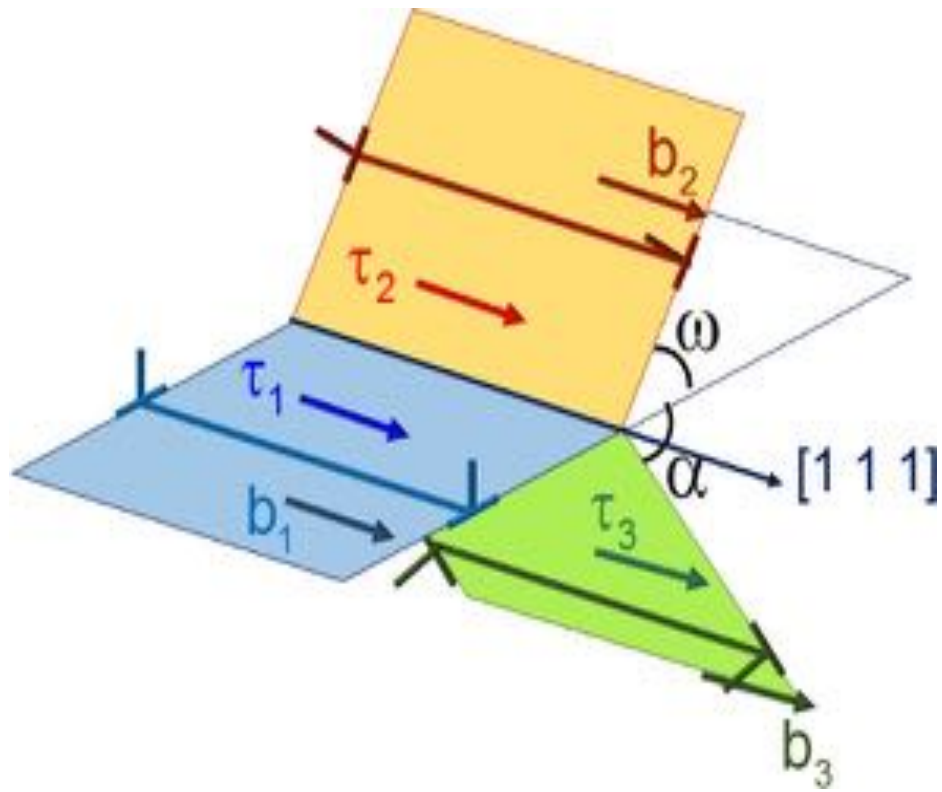


**Figure 5** shows the geometry of the leading partial core and the resolved shear stresses  $\tau_1$ ,  $\tau_2$  and  $\tau_3$  acting on the core fractionals.

$E_{\text{total}}$  is expressed in Eq.(9) as a combination of: (i) the line energies of the fractional dislocations posited inside the core,  $E_{\text{fractional}}$ , (ii) the interaction energies of these fractional dislocations,  $E_{\text{inter-frac}}$ , (iii) the misfit energy associated with the generalized stacking faults formed on the conjugate {112} and/or {110} planes:  $E_{\text{misf}}$ . It should be emphasized that the values of these energy terms are governed by the splitting configuration favored upon the minimization of  $E_{\text{total}}$ .

$$E_{\text{line,1}} = E_{\text{fractional}} + E_{\text{inter-frac}} + E_{\text{misf}} = \sum_{j=1}^3 E_{\text{fractional},j} + E_{\text{inter-frac}} + E_{\text{misf}} \quad (9)$$

The term  $E_{\text{fractional}}$  is comprised of the summation of the line energies associated with three fractional dislocations inside the leading partial and it is expressed as :

$$E_{\text{fractional}} = \sum_{j=1}^3 E_{\text{fractional},j} = \frac{K_b}{4\pi} (b_1^2 + b_2^2 + b_3^2) \ln\left(\frac{R}{\xi}\right) \quad (10)$$

ensuring the conservation of the Burgers vector of the leading partial as expressed in Eq.(11):

$$\sum_{j=1}^3 b_j = b = |a/4 \langle 111 \rangle| \quad (11)$$

On the other hand, the interaction energy associated with the interplay of the elastic fields of these three core fractional dislocations are expressed as [50]:

$$E_{\text{inter-frac}} = \frac{K_{\text{interaction}}}{4\pi} \left( b_1 b_2 \ln \left[ \frac{R^2}{y_1^2 + y_2^2 + y_1 y_2} \right] + b_1 b_3 \ln \left[ \frac{R^2}{y_1^2 + y_3^2 + y_1 y_3} \right] + b_2 b_3 \ln \left[ \frac{R^2}{y_2^2 + y_3^2 + y_2 y_3} \right] \right) \quad (12)$$

A major point to emphasize is that the anisotropic elastic interaction coefficient  $K_{\text{interaction}}$  appearing in Eq.(12) is different from  $K_b$  as the glide planes of the interacting fractional dislocations are not necessarily parallel and may exhibit different crystallographic symmetries along the directions normal to glide direction  $\langle 111 \rangle$ . A detailed insight for the evaluation of  $K_{\text{interaction}}$  parameter is provided in Appendix A based on the anisotropic Eshelby-Stroh method [51-53].

In order to determine the misfit energy of the stacking faults inside the leading partial core separating the fractional dislocations, we need to introduce the mathematical expressions for the disregistry functions  $\{f(x_i)\}$  on the conjugate planes. The functions  $f(x_i)$  are the generalized forms of the  $u_x$  parameter in Figure 1 which account for the spatial variation of the slip in defects particularly the localization effects in dislocations, and allow us to relate the GSFE value to the spatial coordinates  $x_i$  such that  $\gamma(u_x) = \gamma(f(x_i))$ . The non-planar disregistry distribution within the core region of the leading partial is described based on a general form initially proposed by Foreman et al.[54] and Lejcek et al. [55] which is expressed in Eq.(13).

$$f_i(x_i) = b_i + c_i \xi \left( \tan^{-1} \left( \frac{y_i - x_i}{\xi} \right) - \tan^{-1} \left( \frac{y_i}{\xi} \right) \right) \quad (i=1,2,3) \quad (13)$$

The parameters  $c_i$  are determined by the set of boundary conditions expressed in Eq.(14) and (15). Among these two expressions, Eq.(14) indicates that the value of the disregistry functions  $f_i(x_i)$  correspond to the fractional Burgers vectors,  $b_i$ , at the dislocation line position  $x_i = 0$ . On the other hand, Eq.(15) implies that the localized slip present at the core center attenuates at far-field as  $x_i \rightarrow \infty$ .

$$f_i(0) = b_i \quad (14)$$

$$\lim_{x_i \rightarrow \infty} f_i(x_i) = 0 \quad (i=1,2,3) \quad (15)$$

By solving Eq.(12) and (13) simultaneously, the  $c_i$  parameters are evaluated to be as:

$$c_i = \frac{b_i}{\xi \left[ \tan^{-1} \left( \frac{y_i}{\xi} \right) + \frac{\pi}{2} \right]} \quad (16)$$

Following the introduction of the disregistry function formalism, the misfit energy inside the leading partial core,  $E_{\text{misf}}$ , is expressed in a convergent serial form presented in Eq. (17) [56, 57]:

$$E_{\text{misf}} = \sum_{i=1}^3 \sum_{m=-\infty}^{\infty} \gamma_i(f_i(ma' - y_i)) a' \quad (17)$$

In the expression of  $E_{\text{misf}}$ , the first summation on the right hand side is taken over the three conjugate planes on which the dislocation core spreads whereas the second sum represents the collection of the fault energy along each atomic row separated by a distance of  $a'$ . To that end, Eq.(17) accounts for the discrete structure of the lattice by expressing  $x_i$  coordinate as  $ma' - y_i$ . The equilibrium of the four  $a/4$   $\langle 111 \rangle$  partials under either zero or finite external stress necessitates the minimization of the total energy expression given in Eq.(4) which is detailed through Eq. (5)-(17). This implies the determination of the Burgers vectors, i.e.  $b_1, b_2$  ( $b_3$  is given as  $b_3 = b - b_1 - b_2$ ) and the positions of the fractionals, i.e.  $y_1, y_2$  and  $y_3$ , inside the core region of the leading partial.

#### 2.4 Solution Strategy

To solve for the positions of the fractionals  $\{y_1, y_2, y_3\}$  and the Burgers vectors  $\{b_1, b_2, b_3\}$ , we minimized  $E_{\text{tot}} : E_{\text{tot}}(y_1, y_2, y_3, b_1, b_2, b_3)$  via ensuring the equilibrium of fractional dislocations is ensured. The set of three equations which impose the equilibrium of the  $i^{\text{th}}$  fractional dislocation under external stress is written in Eq. (18) as follows:

$$\frac{\partial E_{tot}}{\partial y_i} = 0 \quad (i=1,2,3) \quad (18)$$

Furthermore, the constraint presented in Eq. (19) imposes that the summation of the fractional Burgers vector should result into the leading partial Burgers vector,  $b$ :

$$\sum_{i=1}^3 b_i = b \quad (19)$$

and results in 3 additional equations with an unknown Lagrange multiplier of  $\mu$  such that :

$$\nabla_{b_i} E_{tot} + \mu \nabla_{b_i} \left[ \sum_{i=1}^3 b_i \right] = 0 \quad (20)$$

In Eq. (20),  $\nabla_{b_i} (\cdot)$  is the gradient operator with respect to the fractional Burgers vector  $b_i$ . Given the set of 7 equations in Eq.(18)-(20), the set of 7 unknowns of  $\{y_1, y_2, y_3, b_1, b_2, b_3, \mu\}$  are solved numerically.

The expression of  $E_{tot}$  is denoted as "stable" up until the inactive constraints can be ensured in response to the proportional increase of  $\Sigma$  components. On the other hand, incremental loading physically tends to drive Burgers vectors of the fractional dislocations  $b_2$  and  $b_3$  into the unphysical negative sign domain and results in ill-conditioning [58]. Therefore, the maximum value of glide stress  $\Sigma_{23}$  at which the presence of the local minimum of  $E_{tot}$  is ensured under the prescribed constraint corresponds to the CRSS level.

The solution strategy adopted herein differs from the minimization of the total energy functional proposed earlier for calculating the core configuration of  $a/2 \langle 111 \rangle$  dislocations in pure bcc metals [59, 60]. In that earlier approach,  $\rho_i(x_i)$  distributions on the conjugate planes are evaluated based on the integro-differential Peierls-Nabarro equation. In this work, the fractional dislocation concept is employed to transform the problem of energy functional minimization into a constrained minimization problem of differential calculus. The underlying reason for constructing a different strategy is that the interaction of the disregistry distributions on the conjugate planes introduces an irregular singularity. Unlike the weakly singular integral equations of which are known to be solved by iterative singular value decomposition techniques [61], the existence of solutions for the non-linear, irregularly singular integro-differential equations within the presence of external stress tensor components is not guaranteed [62]. To that end, constraint minimization of  $E_{tot}$  is employed within the framework of the set of equations expressed in Eq.(4)-(20).

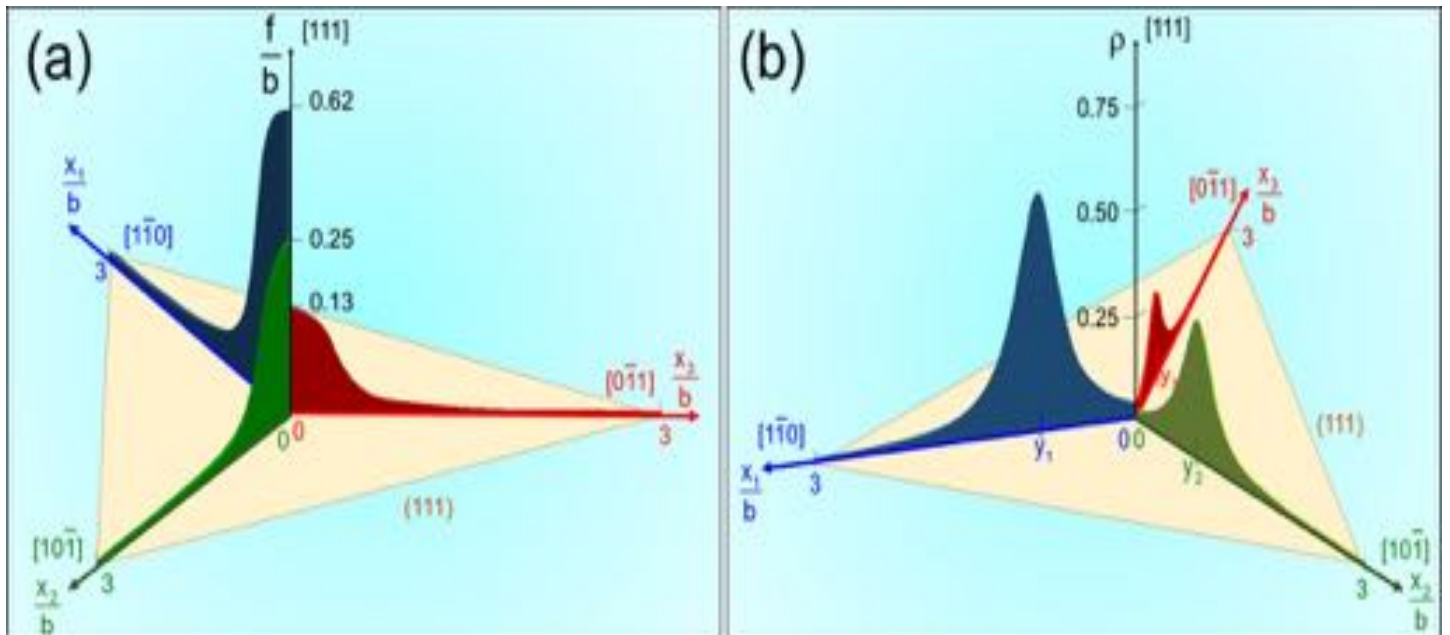


**Figure 3 (a)** illustrates a non-planar core configuration extending on  $(-1-1\ 2)$ ,  $(-2\ 11)$  and  $(1\ -2\ 1)$  planes. The resultant disregistry of the distributions  $f_i$  on each plane correspond to the partial dislocation Burgers vector  $b$ . **(b)** shows the infinitesimal dislocation density  $\rho_i$  which is determined based on the spatial gradient of  $f_i$  field on each plane. The geometric center of  $\rho_i$ , i.e.  $y_i$ , indicates the position of the fractional dislocations with the Burgers vector of  $b_i = \max(f_i)$ .

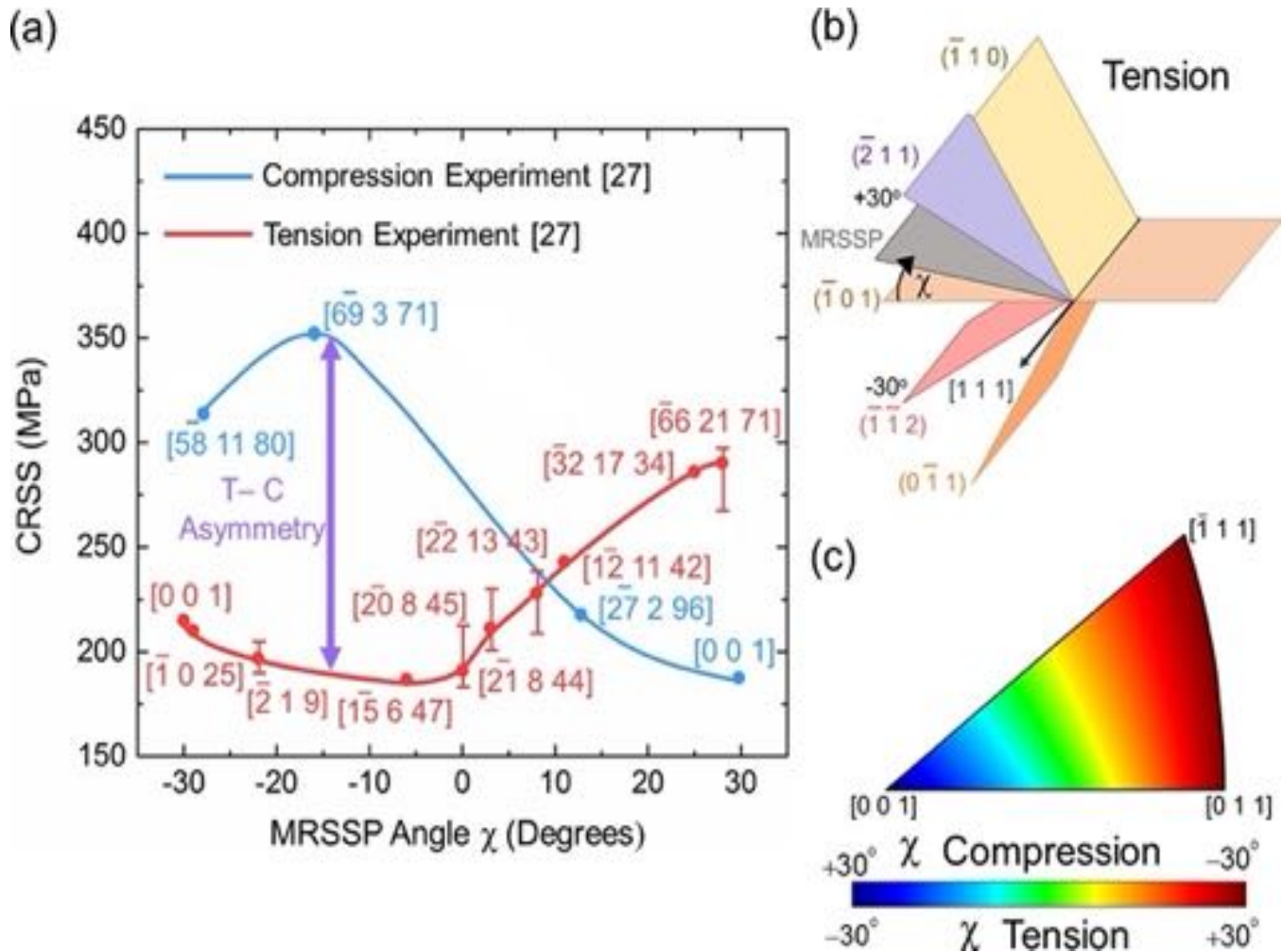


**Figure 6** (a) shows the variation of the experimental CRSS values under uniaxial tension and compression at 323 K [27]. It is to be noted that the abbreviation of "T-C" stands for "tension-compression". (b) illustrates the geometrical interpretation of  $\chi$  angle for uniaxial tension. (c) shows the variation of  $\chi$  angle on the stereographic triangle for  $[111]$  slip direction under uniaxial tension and compression respectively. It is to be noted that in the convention employed, the  $\chi$  value is positive towards the uniaxial tension (compression) orientations favoring the shear along  $\langle 111 \rangle \{112\}$  systems with in the active glide zone in anti-twinning (twinning) sense.

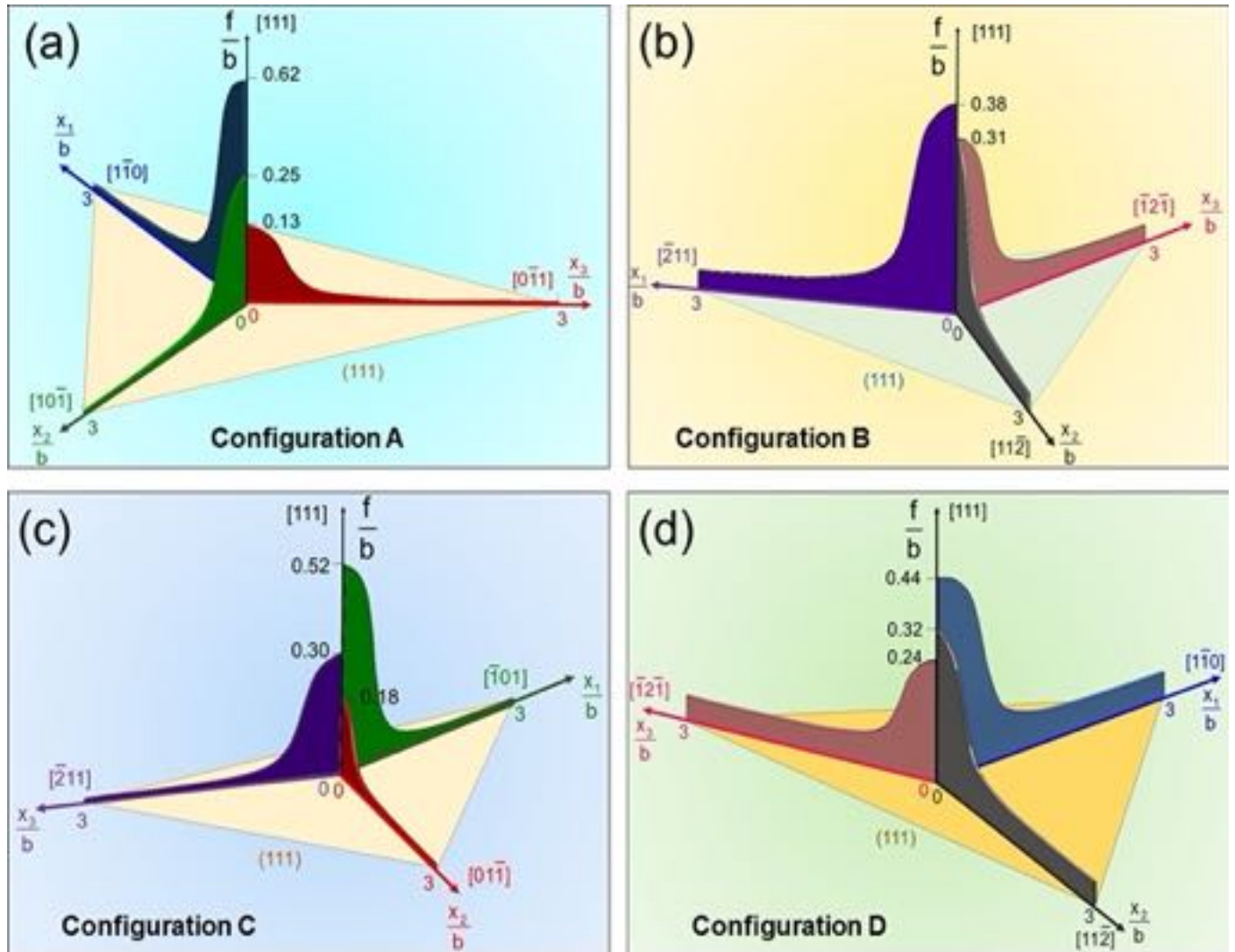


**Figure 7** shows the sessile, externally stress-free core configurations which are grouped into four categories based on the number and the type of planes on which the fractionals are posited. **(a)** shows the leading core configuration split on only  $\{112\}$  planes, i.e. configuration A. **(b)** illustrates the sessile core split on  $\{110\}$  planes only, i.e. configuration B. **(c)** exhibits the core configuration in which fractionals split on two  $\{112\}$  planes and a single  $\{110\}$  plane, configuration C. In **(d)**, the core fractionals prefer to split on a single  $\{112\}$  plane and two  $\{110\}$  planes, i.e. configuration D.

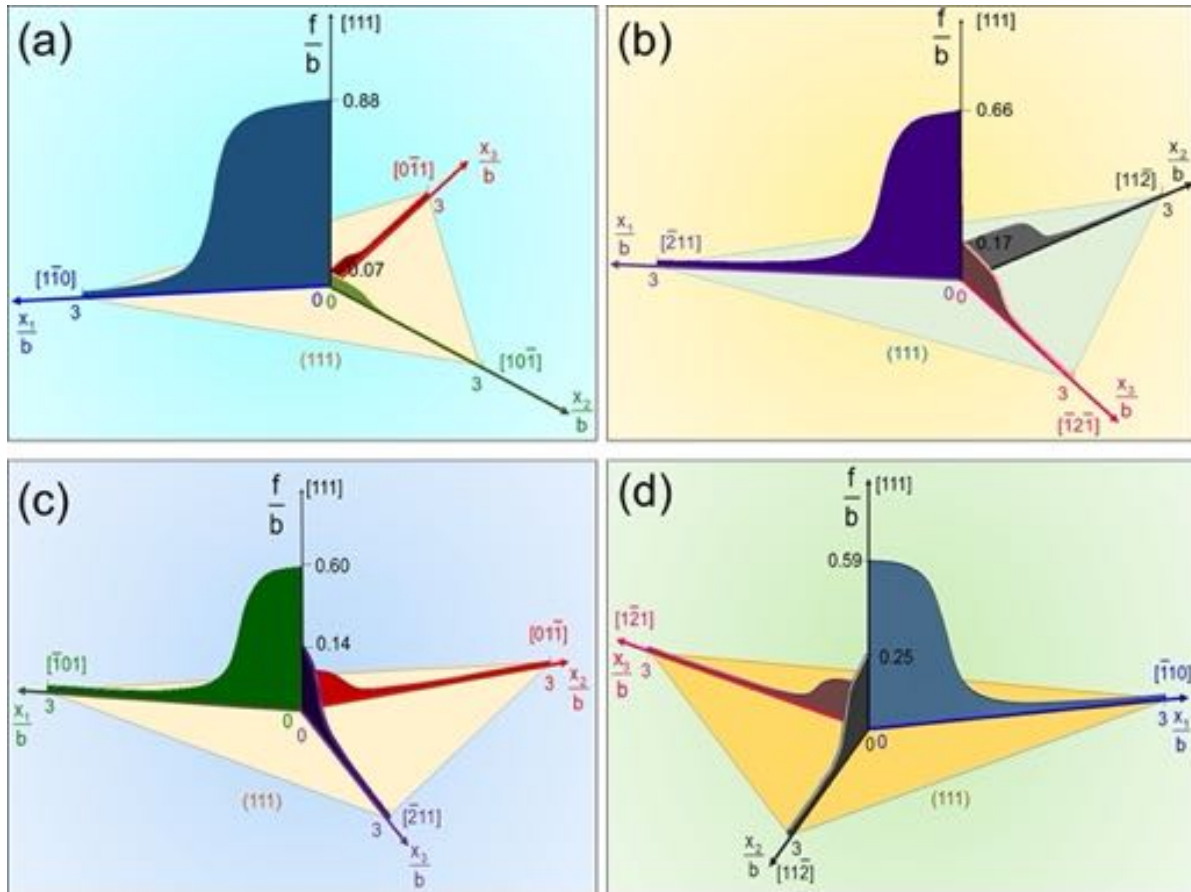


**Figure 8** shows the theoretical variation of the disregistry distributions inside the non-planar core structure of  $a/4$   $[111]$  screw dislocation posited in a uniaxial tension specimen of  $\mathbf{E}_1 - \mathbf{E}_2 - \mathbf{E}_3 = [5\ 8\ 0] - [0\ 0\ 1] - [8\ -5\ 0]$  orientation. **(a)**-**(b)**-**(c)** and **(d)** shows the disregistry distributions evaluated based on the initial core configurations of A-B-C-D in Figure 3. As can be seen the greatest disregistry distribution is observed for the configuration A on  $(-1\ -1\ 2)$   $[111]$  glide system complying with the experimentally reported active slip system [27].

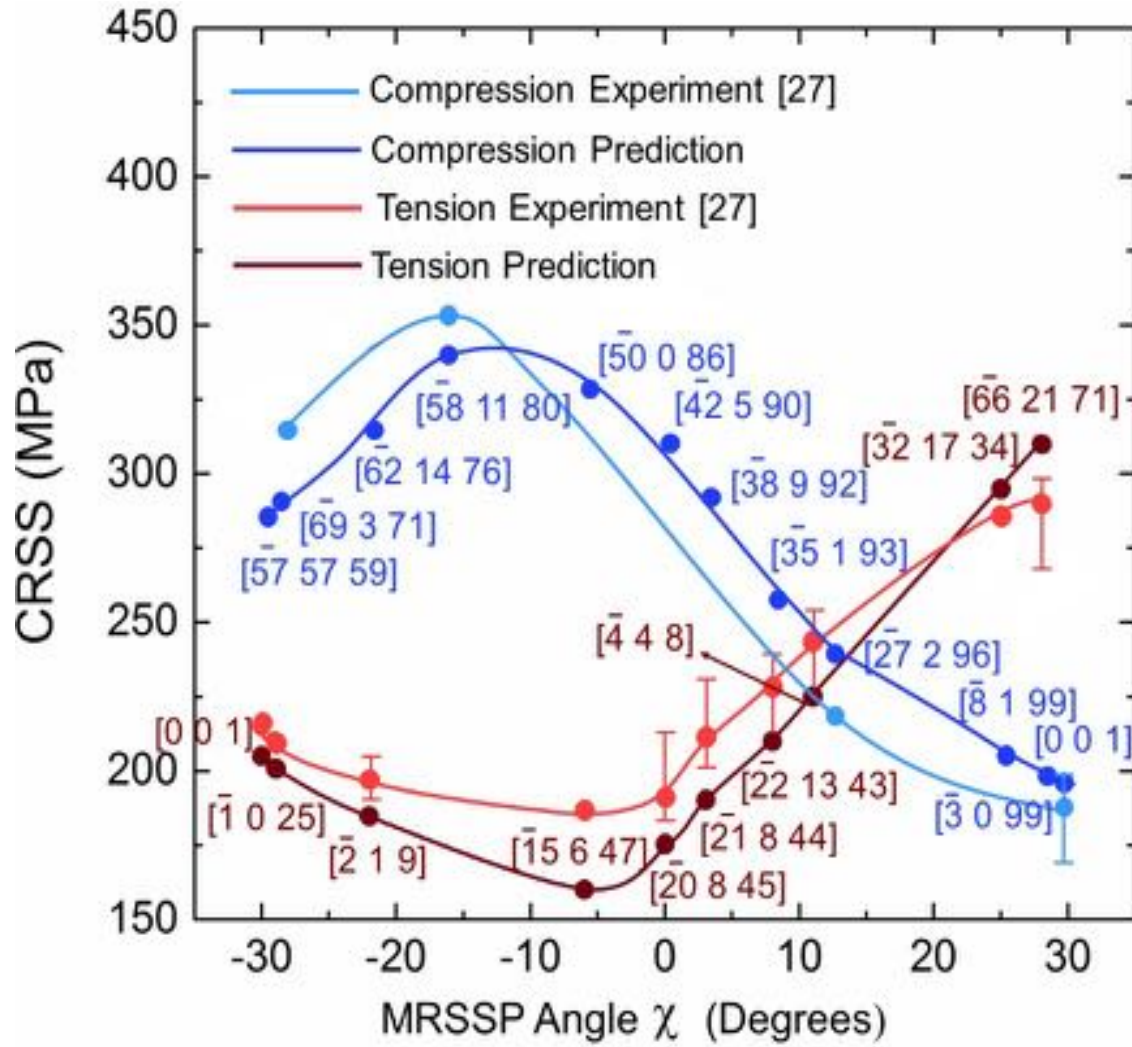


**Figure 9** shows the theoretical CRSS values within range of  $\chi = -30^\circ$  and  $+30^\circ$  under uniaxial tension and compression. The experimental CRSS measurements of Romero et al. [27] (at 323 K) are also included for comparison purposes.

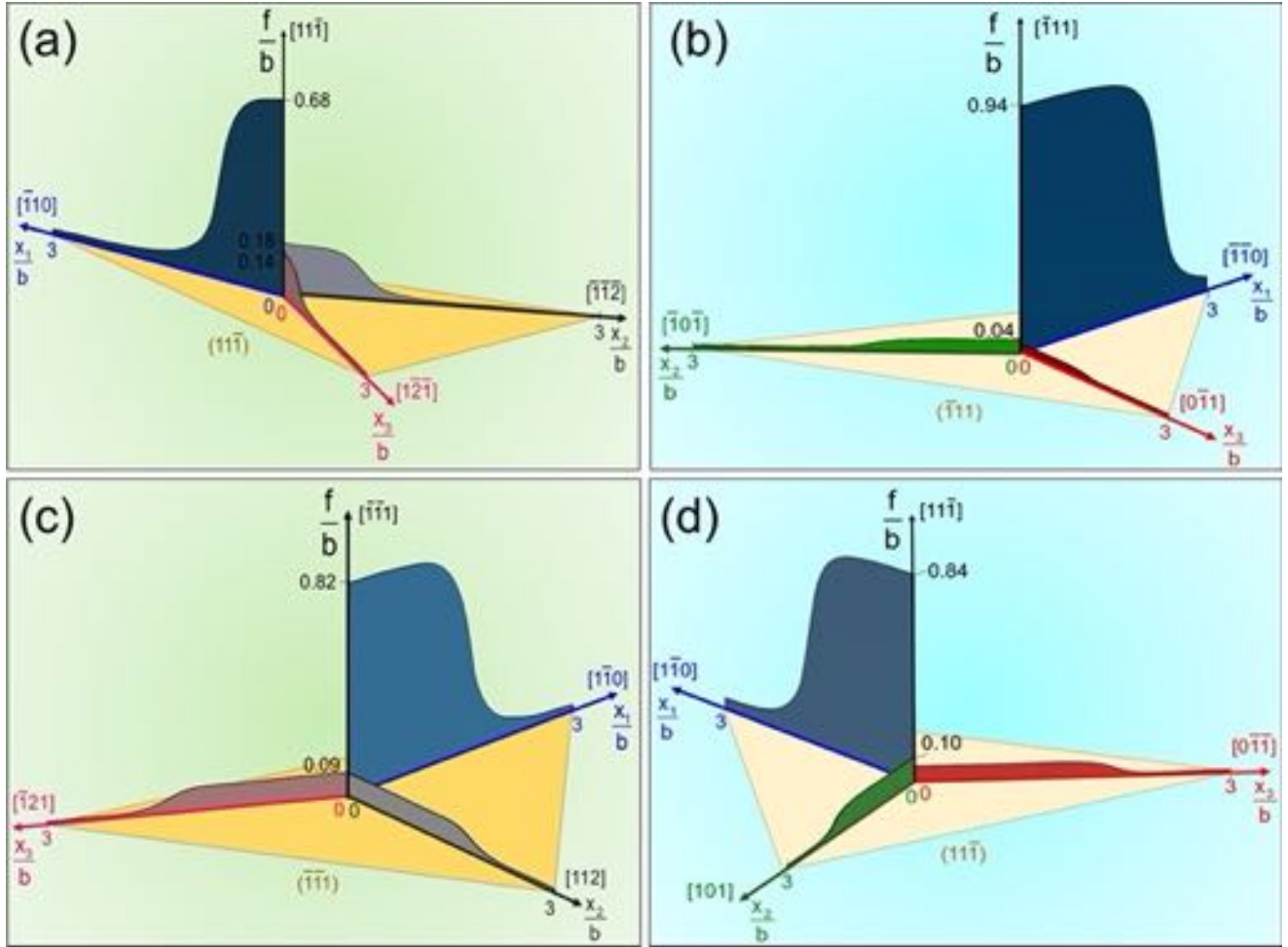


**Figure 10** (a) shows the disregistry distribution inside the leading partial core evaluated for the [-58 11 80] sample under uniaxial compression at the instant of glide initiation. Similarly, (b) shows the disregistry distribution evaluated for the [-15 6 47] sample under uniaxial tension. As can be seen by comparing the core configurations shown in (a) and (b), the transferability of the non-planar disregistry distribution into a planar shape is of paramount importance governing on the experimental and the theoretical CRSS values plotted in Figure 9. The non-planar core shape of the leading partial posited in the [-58 11 80] compression sample introduces an increase of 175 MPa in the CRSS level compared to the [-15 6 47] tension sample which is in line with the experimental 165 MPa difference. On the other hand, the CRSS values are very close, by only 10 MPa, for the [-4 4 8] tension and the [-27 2 96] compression samples of which the core disregistry distributions at the instant of glide initiation are plotted in (c) and (d) respectively. As can be seen in (c) and (d), the disregistry distributions are very similar for both samples. The underlying reason for the minor difference in CRSS levels can be attributed to the GSFE profiles of  $\langle 111 \rangle \{110\}$  and  $\langle 111 \rangle \{112\}$  planes which contribute to  $E_{\text{tot}}$  as manifested in a detailed fashion in *Methods and Theoretical Background* section.

### Construction of a Yield Surface for the Generalized Stress States

Following the theoretical efforts in modelling the anisotropic glide behavior of CuZnAl in the previous sections; we established a compact, analytical yield criterion as a function of the theoretical external stress tensor components at the instant of plastic flow. Broadly speaking, this approach allows to generate a closed form expression serving as a quantitative tool for identifying the slip initiation in CuZnAl alloy within the framework of a macroscale crystal plasticity perspective. To accomplish this task, we incorporated the independent deviatoric stress tensor components  $\mathbf{S}_i$  ( $i,j=1,2,3$ ) which are defined as  $\mathbf{S}_i = \Sigma_i - 1/3\text{trace}(\Sigma)\delta_{ij}$  ( $\delta_{ij}$ :Kronecker Delta), into a linear expression presented in Eq. (21). The coefficients  $\tau_{cr}$  and  $a_i$  ( $i=1,2,3,4$ ) are evaluated by multi-linear regression of the theoretical deviatoric stress components. The resulting yield surface is plotted in Figure 11.

$$\tau_{cr} = S_{23} + a_1 S_{21} + a_2 S_{11} + a_3 S_{22} + a_4 S_{13} \quad (21)$$

$\tau_{cr}$	$a_1$	$a_2$	$a_3$	$a_4$
260	0.85	0.71	0.56	0.25

**Table 3** tabulates the coefficients generating the generalized yield surface plotted in Figure 11, i.e.  $\tau_{cr}$ ,  $a_1$ ,  $a_2$ ,  $a_3$  and  $a_4$ . The coefficients are evaluated based on multi-variable regression of the theoretical deviatoric stress components at the instant of glide initiation at which  $\Sigma_{23}=S_{23}=\text{CRSS}$ .

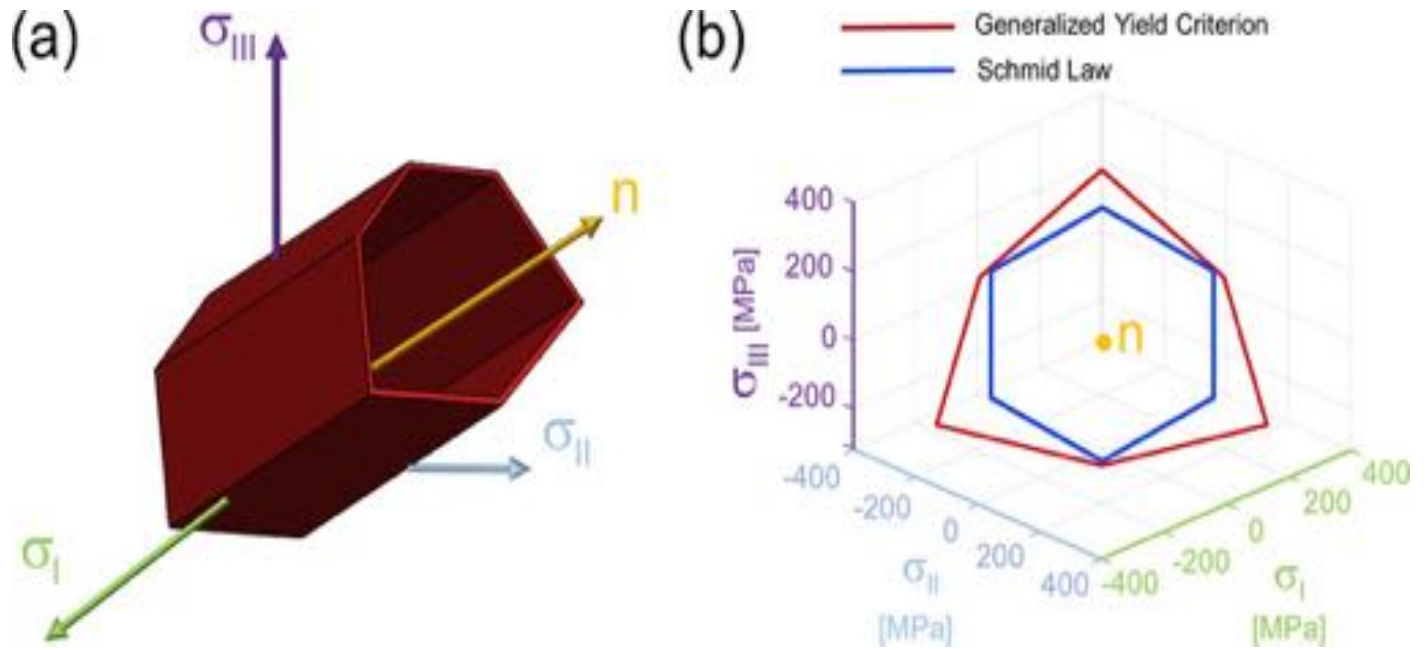


**Figure 11** (a) illustrates the predicted yield hypersurface in the principal stress space. Complying with the previous studies [5, 67], the predicted yield surface is of cylindrical topology with a symmetry axis of  $\mathbf{n} = \Gamma[1,1,1]$ . (b) shows the yield surface projection on the  $\mathbf{n}$ -plane which is normal to  $\mathbf{n}$  vector. As can be seen, significant asymmetry is present in the generalized yield surface suggesting the major deviations from the conventional Schmid Law.

	Configuration A	Configuration B	Configuration C	Configuration D
$b_1$	0.62 b	0.38 b	0.44 b	0.52 b
$b_2$	0.13 b	0.31 b	0.24 b	0.18 b
$b_3$	0.25 b	0.31 b	0.32 b	0.30 b
$y_1$	1.56 b	1.20 b	1.38 b	1.22 b
$y_2$	0.60 b	1.05 b	0.98 b	0.84 b
$y_3$	0.25 b	1.05 b	1.16 b	1.06 b
$E_{\text{tot}}$ (nJ/m)	12.74	13.56	13.19	12.97

**Table 2** tabulates the maximum values of the disregistry distributions of  $f_i(x_i)$  ( $i=1,2,3$ ), namely the Burgers vector of each fractional split on either  $\{110\}$  or  $\{112\}$  conjugate planes, i.e.  $b_i$ , inside the core region of the leading  $a/4$   $[111]$  partial as well as the fractional positions,  $y_i$ , and the total energy values.

Uniaxial Compression			
$\chi$	$\mathbf{E}_1\text{-}\mathbf{E}_2$	$\mathbf{e}_2\text{-}\mathbf{e}_3$	Active Configuration
-29.7°	[1 1 0]-[-57 57 59]	[1 2 3] -[1 1 -1]	D
-28.7°	[1 23 0]-[-69 3 71]	[1 -2 3]-[1 -1 -1]	C
-21.54°	[0 38 -7]-[-62 14 76]	[1 -2 3]-[1 -1 -1]	C
-16.26°	[11 58 0]-[-58 11 80]	[1 2 3] -[1 1 -1]	D
-6.11°	[43 0 25]-[-50 0 86]	[0 1 1]-[1 1 -1]	B
0°	[0 -18 1]-[-42 5 90]	[1 -2 -1]- [1 1 -1]	A
3.13°	[3 19 0]-[-38 6 92]	[1 -2 -1] -[1 1 -1]	A
7.61°	[1 35 0]-[-35 1 93]	[1 -2 -1] -[1 1 -1]	A
12.68°	[2 27 0]-[-27 2 96]	[1 -2 -1] -[1 1 -1]	A
25.02°	[1 8 0]-[-8 1 99]	[1 -2 -1]- [1 1 -1]	A
28.3°	[33 0 1]-[-3 0 99]	[-1 2 -1] -[-1 -1 -1]	A
30°	[0 1 0]-[0 0 1]	[-2 1 1] -[-1 -1 -1]	A

**Table B.1** The characteristic angle  $\chi$  the crystallographic directions parallel to the sample frame base vectors  $\mathbf{E}_1\text{-}\mathbf{E}_2$  and the dislocation frame base vectors  $\mathbf{e}_1\text{-}\mathbf{e}_2$  are tabulated for the uniaxial compression loading acting in line with  $\mathbf{E}_2$  along with the favored configuration, i.e. either A, B, C or D.

Uniaxial Tension			
$\chi$	$\mathbf{E}_1\text{-}\mathbf{E}_2$	$\mathbf{e}_2\text{-}\mathbf{e}_3$	Active Configuration
-30°	[5 8 0]-[0 0 1]	[-1 -1 2]-[1 1 1]	A
-28.6°	[7 3 0]-[-1 0 25]	[1 1 2]-[-1 -1 1]	A
-22.43°	[9 1 1]-[-2 1 9]	[1 -1 2]-[-1 1 1]	A
-5.52°	[2 5 0]-[-15 6 47]	[1 -1 2]-[-1 1 1]	A
-0.15°	[2 5 0]-[-20 8 45]	[1 -1 2]-[-1 1 1]	A
2.93°	[0 -11 2]-[-21 8 44]	[0 1 1]-[-1 -1 1]	B
7.71°	[0 -43 13]-[-22 13 43]	[0 1 1]-[-1 -1 1]	B
10.89°	[1 1 0]-[-4 4 8]	[-1 3 2]-[-1 -1 1]	D
25.12°	[0 2 -1]-[-32 17 34]	[-1 3 2]-[-1 -1 1]	D
27.81°	[7 22 0]-[-66 21 71]	[-1 3 2]-[-1 -1 1]	D

**Table B.2** The characteristic angle  $\chi$ , the crystallographic directions parallel to the sample frame base vectors  $\mathbf{E}_1\text{-}\mathbf{E}_2$  and the dislocation frame base vectors  $\mathbf{e}_1\text{-}\mathbf{e}_2$  are tabulated for the uniaxial tension loading acting in line with  $\mathbf{E}_2$  along with the favored configuration, i.e. either A, B, C or D.



Contents lists available at ScienceDirect

## Journal of the Mechanics and Physics of Solids

journal homepage: [www.elsevier.com/locate/jmps](http://www.elsevier.com/locate/jmps)

# The complexity of non-Schmid behavior in the CuZnAl shape memory alloy

S. Alkan, A. Ojha, H. Sehitoglu\*

Department of Mechanical Science and Engineering, University of Illinois at Urbana-Champaign, 1206W. Green Street, Urbana, IL 61801, USA

## ARTICLE INFO

## Article history:

Received 1 September 2017  
 Revised 20 February 2018  
 Accepted 26 February 2018  
 Available online 27 February 2018

## ABSTRACT

The paper addresses one of the most important yet overlooked phenomenon in shape memory research- the plastic slip response. We show that the slip response is highly crystal orientation dependent and we demonstrate the precise reasons behind such complex response. The fractional dislocations on  $\langle 111 \rangle \{112\}$  or  $\langle 111 \rangle \{011\}$  systems can be activated depending on the sample orientation and solutions are derived for the variations in disregistry and dislocation core spreadings. This leads to the calculation of critical resolved shear stress in close agreement with experimental trends. The results show considerable dependence of the flow behavior on the non-Schmid stress components and the proposed yield criterion captures the role of stress tensor components.

© 2018 Elsevier Ltd. All rights reserved.

## 1. Introduction

The plastic deformation of shape memory alloys remains one of the most intriguing topics of research because the yielding behavior does not follow the well-known Schmid law that has been primarily developed for face centered cubic (fcc) and hexagonal close packed (hcp) metals (Schmid and Boas, 1950). Most shape memory alloys have an austenitic cubic structure such as a B2 or L2<sub>1</sub>, (i.e. ordered lattices) and undergo slip in {011} and/or {112} planes (Otsuka and Wayman, 1998; Chowdhury and Sehitoglu, 2016). A noteworthy observation is that because the dislocation core spreading occurs on conjugate slip planes, the description of the plastic flow must account for non-glide stress components (Alkan and Sehitoglu, 2017). Consequently, the description of yielding for plasticity at the crystal lattice level must embrace a form that departs from the well-known Schmid law. Recent research results and simulation efforts have focused on Fe<sub>3</sub>Al (Alkan and Sehitoglu, 2017) and NiTi (Alkan et al., 2017; Alkan and Sehitoglu, 2017), and for the first time a new yield criterion was proposed accounting for non-glide stresses for these two ordered shape memory alloys at the crystal level. Before expounding on the details of the non-Schmid behavior in shape memory alloys, we provide an overview of the flow behavior in body centered cubic (bcc) materials.

Dating back to the early experiments of Taylor (1928) the complicated plastic deformation behavior of bcc metals and alloys has been of interest for numerous researchers (Vitek, 1974; Basinski et al., 1981; Duesbery, 1984; Duesbery, 1984; Yamaguchi and Umakoshi, 1983; Sherwood et al., 1967; Gröger et al., 2008; Gröger et al., 2008; Lin et al., 2012). With the emergence of the atomistic scale simulation capabilities in the late sixties (Chang, 1967; Vitek, 1968; Duesbery et al., 1973; Suzuki, 1968), the dislocation core structure and short range interatomic forces are determined to be responsible for this experimentally observed complexity. On the other hand, the studies in the last three decades have undoubtedly shown that

\* Corresponding author.

E-mail address: [huseyin@illinois.edu](mailto:huseyin@illinois.edu) (H. Sehitoglu).

the screw dislocations inside the bcc-based ordered lattice structures generally exhibit strong deviations from the critical resolved shear stress (CRSS) law (also known as Schmid Law (Schmid and Boas, 1950)), especially at low temperatures (Christian, 1983; Vitek, 1985). Recent experimental work and atomistic calculations report that shape memory alloys show pronounced deviations from Schmid Law owing to the strongly anisotropic nature of the interatomic forces persisting at finite temperatures (Alkan and Sehitoglu, 2017; Alkan et al., 2017; Hu et al., 2006). As Cu based shape memory alloys are finding more application fields owing to their cheaper cost, considerable transformation strain and high thermal/electrical conductivities (Otsuka and Wayman, 1998; Sutou et al., 2008; Wayman, 1980; Gautier and Patoor, 1997; Wu, 1990); in this work, we interrogated on the plastic deformation characteristics of L<sub>21</sub> ordered ternary CuZnAl (21.6 at. % Zn–13.15 at. % Al) alloy (Romero et al., 1988), briefly denoted as CuZnAl hereinafter, within the framework of *ab-initio* and continuum scale calculations.

In contrast with the close packed pure metals in which the slip motion is dictated by a unique CRSS value along the densest atomic direction - except the pyramidal and prismatic glide in hcp metals (Vitek, 1985), the glide resistance in bcc based structures exhibit strong interplay with the applied stress state in both pure metals and alloys (Duesbery and Vitek, 1998; Vitek and Paidar, 2008). This interaction leads to the non-unique CRSS values which are dependent on the external stress tensor. Complying with this hypothesis, earlier literature on CuZnAl addresses that significant CRSS differentials can be observed as a function of the single crystal orientation under uniaxial loading (Romero et al., 1988). The plastic deformation of CuZnAl is accommodated by the glide of super-lattice dislocations of a  $\langle 111 \rangle$  type tending to glide on  $\{110\}$  and  $\{112\}$  planes (a is the lattice constant of CuZnAl  $5.828 \text{ \AA}$  (Wu et al., 2015)) (Jara et al., 1985). Furthermore, this super-lattice dislocation dissociates into the four partial dislocations of each having  $a/4 \langle 111 \rangle$  Burgers vector. The partials are joint by the Nearest Neighbor (NN) and Next Nearest Neighbor (NNN) Antiphase boundary (APB) faults which are formed due to the change in NN and NNN lattice sites of L<sub>21</sub> ordered crystal structure.

Previous studies in the literature indicate that the core structure of the screw character partials in L<sub>21</sub> ordered lattices exhibit non-planar extension on  $\{110\}$  and/or  $\{112\}$  family planes within the glide zone of  $\langle 111 \rangle$  (Yamaguchi and Umakoshi, 1983; Duesbery and Richardson, 1991). The distribution of slip inside the non-planar core structure is surmised to exhibit strong interplay with the external stress tensor and therefore results in deviations from the Schmid Law complying with the experimental observations (Romero et al., 1988). In the sequel, we would like to develop a quantitative understanding to predict the non-unique CRSS values in CuZnAl. To that end, we probed the interaction between the screw dislocation core shape and the external stress state within the framework of a multiscale (atomistic-continuum) slip energetics formulation. To accomplish this task, we generated the GSFE profiles along the  $\langle 111 \rangle \{110\}$  and  $\langle 111 \rangle \{112\}$  glide systems via *ab-initio* calculations. Adopting these GSFE profiles into the total energy formulation of a dissociated a  $\langle 111 \rangle$  super-lattice screw dislocation, we constructed a solution algorithm contingent on the constrained minimization of the total energy expression. The calculations employ the anisotropic dislocation theory (Steeds, 1973; Hirth and Lothe, 1968) and encompasses the contribution of both four  $a/4 \langle 111 \rangle$  partials and the fractional dislocations inside the leading partial core on the CRSS values for slip. Within these efforts, the non-planar core structure of the leading partial plays a key role. To that end, the possible leading core configurations under external stress are also incorporated into the model to capture the core shape in response to the different external stress components. Notably, this theoretical analysis helps pave the way for a deeper comprehension of the interaction between the core configurations and the CRSS levels exhibiting non-Schmid behavior.

Although a rich body of literature surrounds the atomistic-scale core behavior in bcc-based lattice structures; yet much remains to be incorporated into the conventional crystal plasticity calculations to embrace the deviations from the Schmid law. The contribution of the non-glide stress components to the plastic yielding has been addressed for pure bcc metals only within a limited number of studies (Gröger et al., 2008; Patra et al., 2014; Lim et al., 2013; Dao and Asaro, 1993) in spirit of the framework by Qin and Bassani (1992). More recently, the current authors have proposed a generalized yield criterion accounting for the contribution of non-glide stress components (either shear or normal character) to the slip initiation in DO<sub>3</sub> ordered Fe<sub>3</sub>Al and B2 ordered NiTi alloys (Alkan and Sehitoglu, 2017; Alkan et al., 2017; Alkan and Sehitoglu, 2017) as well as in transformation stress of CuZnAl alloy (Alkan et al., 2018). The resulting theoretical predictions exhibit close agreement with the experimental behavior emphasizing the pronounced contribution of the non-glide stresses upon the CRSS levels in ordered shape memory alloys. As a forward step, in this work, we propose a generalized yield criterion based on the theoretical evaluation of the deviatoric stress components corresponding to the glide of a  $\langle 111 \rangle$  super-lattice dislocation in CuZnAl. The resulting theoretical yield surface accomplishes to bridge the atomic scale dislocation core configurations to the macroscopic plastic yield behavior.

In summary, considering the intricate nature of the dislocation mediated slip in CuZnAl; we aim to quantify the slip energetics and develop a theoretical model to predict CRSS values. The model focuses on the stability of the total energy associated with a  $\langle 111 \rangle$  super-dislocation in conjunction with the non-planar core shape of the leading partial. The predicted values are shown to be in close agreement with the systematic experimental measurements presented in the earlier literature (Romero et al., 1988). A discussion on the possible extensions of the proposed plastic glide model for the cyclic and superelastic behavior is also provided.

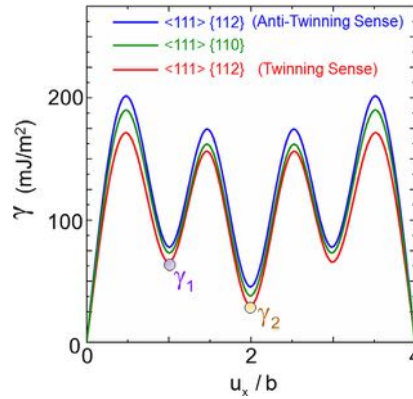


**Fig. 1.** Shows the generalized stacking fault energy (GSFE) curves along  $\langle 111 \rangle \{110\}$  and  $\langle 111 \rangle \{112\}$  slip systems considering the intrinsic asymmetry along the twinning and anti-twinning directions. The disregistry displacement  $u_x$  varies between 0 to a  $|\langle 111 \rangle|$ . The local minima  $\gamma_1$  and  $\gamma_2$  show the stable NNAPB and NNNAPB fault energy levels.

**Table 1**

Tabulation of the NNAPB and NNNAPB energy values, i.e.  $\gamma_1$  and  $\gamma_2$ , respectively, extracted from the GSFE curves of  $\langle 111 \rangle \{112\}$  slip system along the twinning and the anti-twinning directions and  $\langle 111 \rangle \{110\}$  system. The separation distances between the partials under zero external stress, i.e.  $d_1$  and  $d_2$ , are also included. It is to be noted that  $d_1$  and  $d_2$  values on  $\{112\}$  plane are calculated based on the average  $\gamma_1$  and  $\gamma_2$  values of the twinning and the anti-twinning directions.

NNAPB $\gamma_1$ $\langle 111 \rangle \{112\}$ Twinning Sense (mJ/m <sup>2</sup> )	61
NNNAPB $\gamma_2$ $\langle 111 \rangle \{112\}$ Twinning Sense (mJ/m <sup>2</sup> )	26
NNAPB $\gamma_1$ $\langle 111 \rangle \{112\}$ Anti-Twinning Sense (mJ/m <sup>2</sup> )	77
NNNAPB $\gamma_2$ $\langle 111 \rangle \{112\}$ Anti-Twinning Sense (mJ/m <sup>2</sup> )	35
NNAPB $\gamma_1$ $\langle 111 \rangle \{110\}$ (mJ/m <sup>2</sup> )	70
NNNAPB $\gamma_2$ $\langle 111 \rangle \{110\}$ (mJ/m <sup>2</sup> )	31
$d_1$ $\{110\}$ (nm)	2.6
$d_2$ $\{110\}$ (nm)	13.40
$d_1$ $\{112\}$ (nm) (average)	2.7
$d_2$ $\{112\}$ (nm) (average)	13.45

## 2. Methods and theoretical background

### 2.1. Construction of generalized stacking fault energy (GSFE) curves

The uniaxial tension/compression experiments of Romero et al. (1988) conducted within a wide range of single crystal orientations along with the Transmission Electron Microscope (TEM) images address the single or combined activation of  $\langle 111 \rangle \{112\}$ ,  $\langle 111 \rangle \{110\}$  slip systems (Romero et al., 1988; Jara et al., 1985). Based on this experimental evidence, we generated the GSFE curves of CuZnAl alloy along the  $\langle 111 \rangle \{112\}$  and  $\langle 111 \rangle \{110\}$  glide systems by utilizing Vienna ab-initio Simulation Package (VASP) with the projector augmented wave method and generalized gradient approximation (Kresse and Furthmüller, 1996; Kresse and Hafner, 1993). In the simulation procedure, a  $2 \times 7 \times 2$  supercell with 112 atoms is constructed in a  $L2_1$  lattice structure. The simulations are performed using  $12 \times 5 \times 12$  k points for Brillouin zone integration within the framework of Monkhorst Pack meshing procedure. The resulting energy values are ensured to converge within  $10^{-5}$  eV/atom tolerance using conjugate gradient algorithm. An energy cut-off value of 360 eV with plane wave basis set was implemented in the simulations. The atoms are allowed to relax along all but the  $\langle 111 \rangle$  direction. The resulting GSFE curves along the  $\langle 111 \rangle \{110\}$  and  $\langle 111 \rangle \{112\}$  systems- considering the intrinsic asymmetry for the twinning and anti-twinning senses- are shown in Fig. 1.

As can be seen in Fig. 1, the dissociated configuration of a  $\langle 111 \rangle$  dislocation observed in the earlier TEM studies is reflected in the energy profiles of slip along both  $\langle 111 \rangle \{112\}$  and  $\langle 111 \rangle \{110\}$  systems by the four local maxima (Jara et al., 1985; Sade et al., 1987). These local maximum energy barrier values are separated by the stable local minima located at the disregistry levels of  $u_x = (n/4) \langle 111 \rangle$  where  $n = 1, 2, 3$ . For  $n = 1, 3$ ; the local energy minima correspond to NNAPB energy levels, i.e. shown as  $\gamma_1$  in Fig. 1(a); meanwhile NNNAPB energy level corresponds to the local minimum at  $n = 2$  which is denoted as  $\gamma_2$ . The numerical values of these energy levels evaluated via the *ab-initio* calculations are tabulated in Table 1. These APB energy levels are of paramount importance in governing the core configuration of super-lattice partials, with equal Burgers vector of  $\mathbf{b} = a/4 \langle 111 \rangle$  ( $b = |\mathbf{b}|$ ), via exerting restoring forces on them.

The equilibrium separation distances  $d_1$  and  $d_2$  between the screw partials in externally stress free configuration, as illustrated in Fig. 2, are evaluated by the balance of the repulsive dislocation interaction forces with the restoring forces originating from the NNAPB and NNNAPB faults. The stable APB energy values of  $\gamma_1$  and  $\gamma_2$  are related to the distances of

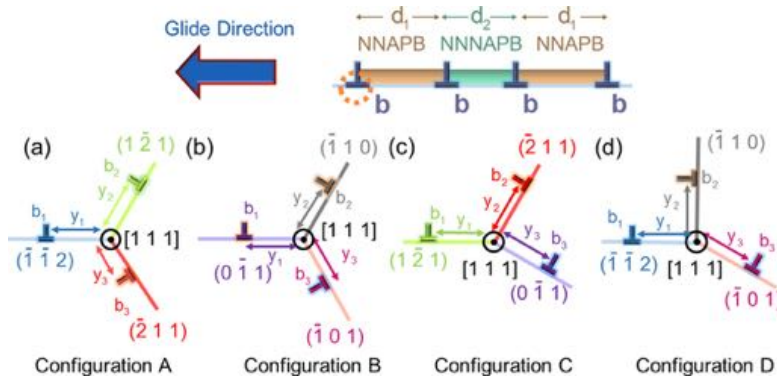


Fig. 2. Shows the possible core configurations of the  $a/4 \langle 111 \rangle$  leading partial in CuZnAl.

$d_1$  and  $d_2$  as (Crawford et al., 1973):

$$\gamma_1 = \frac{K_s b^2}{2\pi} \left\{ \frac{1}{d_1} + \frac{1}{d_1 + d_2} + \frac{1}{2d_1 + d_2} \right\} \quad (1)$$

$$\gamma_2 = \frac{K_s b^2}{2\pi} \left\{ \frac{2}{d_1 + d_2} + \frac{1}{2d_1 + d_2} + \frac{1}{d_2} \right\} \quad (2)$$

The resulting  $d_1$  and  $d_2$  values from the simultaneous solution of the expressions in Eqs. (1) and (2) are tabulated in Table 1 for both  $\{110\}$  and  $\{112\}$  planes.  $K_s$ , appearing in Eqs. (1) and (2), is an anisotropic coefficient dependent on the lattice structure and is equal to 84 GPa (Steeds, 1973; Lothe, 1992; Foreman, 1955). The resulting value of  $d_1$  is in close agreement with the experimental measurement of 3 nm (Romero et al., 1988) justifying the GSFE profile in Fig. 1 generated from the *ab-initio* calculations.

## 2.2. Non-planar core structure of $a/4 \langle 111 \rangle$ partials

The earlier atomistic scale calculations focusing on the dislocation core structure in bcc lattices, have a consensus that the core displacements of  $a/2 \langle 111 \rangle$  screw dislocations mainly extend on  $\{110\}$  planes and no metastable stacking faults are present on the generated GSFE curves along the glide systems (Vitek, 1974; Gröger et al., 2008; Duesbery and Vitek, 1998; Frederiksen and Jacobsen, 2003; Duesberry, 1989). In externally stress-free configuration,  $a/2 [111]$  screw dislocation core in a bcc lattice has been evaluated to exhibit a threefold symmetry (with core spreading on  $(-101)$ ,  $(0-11)$  and  $(-110)$  planes) for the pair (Vitek, 1974.; Vitek et al., 1970) and the Embedded Atom Method [Duesbery and Vitek, 1998; Wang et al., 2001] potentials with two degenerate energetically equivalent structures which are not invariant to  $[-101]$  diad symmetry. On the other hand, recent calculations based on the bond order potentials and first-principles calculations demonstrate a core possessing three-fold symmetry with additional  $[-101]$  diad symmetry operation for  $a/2 [111]$  screw dislocations leading to a non-degenerate structure (Gröger et al., 2008; Woodward and Rao, 2001) (For a review (Vitek and Paidar, 2008)). Generally, within the presence of external stress, the core spreading in a bcc lattice is cast into a more complicated shape which breaks the threefold symmetry along the  $\langle 111 \rangle$  glide zone.

Extending the discussion to the ordered structures, i.e. B2, DO<sub>3</sub> and L2<sub>1</sub>, points out a similar behavior for the screw core to that of the parent bcc lattice only with subtle variations. As a distinguishing point, in these alloy crystallite, the non-planar core structure has the tendency to prevent the overlap with the APB faults to minimize its energy (Duesbery and Richardson, 1991). For L2<sub>1</sub> ordered CuZnAl, the core structure may favor spreading on a combination of  $\{112\}$  and  $\{110\}$  planes depending on the slip energetics and the dislocation formation energy. Furthermore, the external stress tensor is also surmised to play a decisive role in the core spreading. On mechanical grounds, the configuration of the leading partial of  $a/4 \langle 111 \rangle$  Burgers vector is of paramount importance to identify the CRSS required to pinpoint the slip initiation in CuZnAl. To that end, Fig. 2 summarizes the four possible leading core configurations for the particular case of  $a/4 [111]$  leading partial with the corresponding conjugate planes.

Among the core configurations illustrated in Fig. 2, configuration A favors the core spreading on the conjugate  $\{112\}$  family planes in the  $\langle 111 \rangle$  glide zone. Two (one) of these conjugate planes promote glide in twinning (anti-twinning) sense. In configuration B, the core structure is spread on the conjugate  $\{110\}$  planes. The other possible configurations C and D, consist of a core which spreads on a combination of  $\{112\}$  and  $\{110\}$  planes. At this point, it is important to emphasize that the glide resistance in twinning sense on  $\langle 111 \rangle \{112\}$  system is intrinsically lower than the anti-twinning sense. The departure from symmetry in the glide resistance along  $\langle 111 \rangle \{112\}$  system originates from the symmetry group of bcc-based structures and is also reflected in the GSFE curves generated in Fig. 1.

Inside the core of each superpartial, the net  $a/4 \langle 111 \rangle$  Burgers vector is distributed as of registry displacements, parallel to  $\langle 111 \rangle$ , on the conjugate  $\{110\}$  and/or  $\{112\}$  planes (Yamaguchi and Umakoshi, 1983). An example of the non-planar core

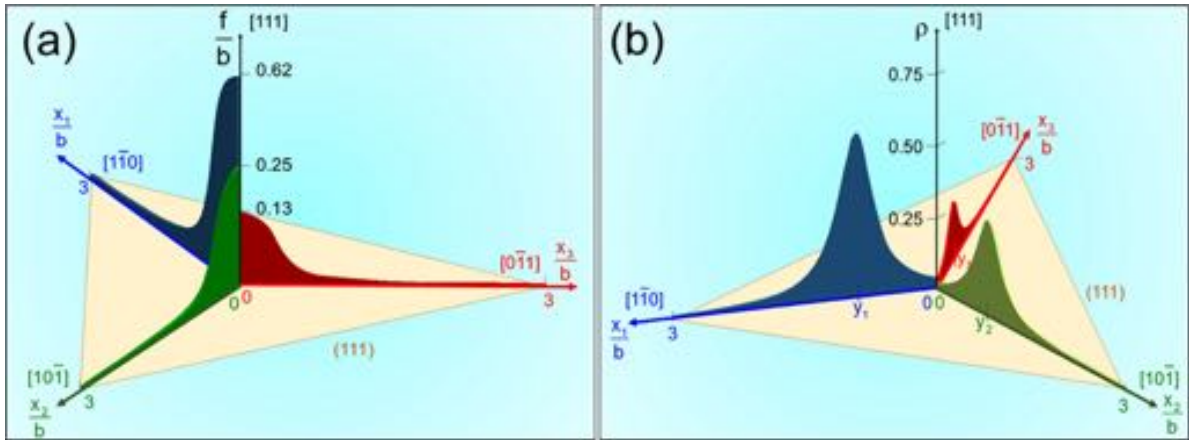


**Fig. 3.** (a) Illustrates a non-planar core configuration extending on  $(\bar{1}\bar{1}2)$ ,  $(\bar{2}11)$  and  $(1\bar{2}1)$  planes. The resultant disregistry of the distributions  $f_i$  on each plane correspond to the partial dislocation Burgers vector  $b$ . (b) shows the infinitesimal dislocation density  $\rho_i$  which is determined based on the spatial gradient of  $f_i$  field on each plane. The geometric center of  $\rho_i$ , i.e.  $y_i$ , indicates the position of the fractional dislocations with the Burgers vector of  $b_i = \max(f_i)$ .

disregistry distributions, denoted as  $f_i$  ( $i=1,2,3$ ), for configuration A of Fig. 2(a) is illustrated in Fig. 3(a). It should be noted that the resultant of these slip distributions on the three conjugate planes sum up to  $b$  at the dislocation line center which corresponds to  $x_i = 0$ . The characteristic features of the  $f_i$  distribution will be further interrogated on mathematical grounds in the subsequent section.

In general, the disregistry displacements inside the non-planar core are identified as generalized stacking faults and do not correspond to a local minimum on the GSFE curve. To that end, these faults exhibit a different character from the partial dislocations which are separated by the stable stacking faults with a constant prescribed slip vectors, i.e. of either NNAPB or NNNAPB faults (Duesbery et al., 1973). Following the nomenclature of the earlier literature, the resultant of these disregistry displacements on each conjugate plane inside the core is denoted as the fractional dislocations (or fractionals) as shown in Fig. 2 (Vitek and Kroupa, 1969). The positions of the fractional dislocations,  $y_i$ , correspond to the geometric center of the infinitesimal-continuous dislocation density of  $\rho_i$  (Eshelby, 1949). From a mathematical perspective,  $\rho_i$  corresponds to the spatial derivative of  $f_i$  distribution (with respect to  $x_i$  coordinate). The Burgers vector of each fractional dislocation is denoted as  $b_i$  -shown in Fig. 2- and equal to the value of  $f_i$  at the dislocation line center -see Fig. 3(a).

### 2.3. Modelling the initiation of glide motion for the leading partial

To initiate the glide motion of the leading partial in CuZnAl under external stress, the fractionals change their positions and the core structure is said to transform from a sessile to a glissile configuration analogous to the  $a/2 \langle 111 \rangle$  dislocation core structure in a pure bcc metal (Kroupa and Vitek, 1967). The positions of the fractionals are highly dependent on the external stress tensor to sustain equilibrium until the resolved shear stress acting on the most favorable slip system reaches a critical value, i.e. CRSS. Beyond this critical stress level, the fractional dislocation subjected to the highest glide force translates by multiple lattice spacings initiating plastic slip. Throughout this section, we will elaborate on developing a mathematical framework which can describe the slip initiation bridging external stress tensor with the core configuration.

Determination of the theoretical CRSS levels requires to incorporate the slip geometry into the total energy expression,  $E_{tot}$ . This formulation incorporates both long-range elastic and short-range misfit energy terms as well as the work done by the external stress components on the dissociated a  $\langle 111 \rangle$  dislocation configuration. To that end, the external stress tensor  $\sigma$  applied on the sample should be described with respect to the dislocation coordinate frame. This task is accomplished by transforming the  $\sigma$  tensor from the sample frame  $X_1 - X_2 - X_3$  to the dislocation frame  $x_1 - x_2 - x_3$ . The base vectors of these two orthonormal coordinate systems are denoted as  $\mathbf{E}_1 - \mathbf{E}_2 - \mathbf{E}_3$  and  $\mathbf{e}_1 - \mathbf{e}_2 - \mathbf{e}_3$  respectively. As illustrated in Fig. 4, these vectors are chosen on purpose in both coordinate frames. Meanwhile,  $\mathbf{E}_2$  coincides with the outwards normal of the surface on which the uniaxial loading is applied; the vectors  $\mathbf{e}_2$  and  $\mathbf{e}_3$  are chosen to be parallel to the active glide plane normal and its Burgers vector respectively. The transformation of the coordinates from the sample to the dislocation frame is accomplished via the orthogonal matrix  $\mathbf{Q}_{ij}$  which is described as  $\mathbf{Q}_{ij} = \mathbf{e}_i \cdot \mathbf{E}_j$  where  $i, j = 1, 2, 3$  ( $\cdot$  is the dot product operator). Following the second order tensor transformation rules, the external stress tensor is transformed to the dislocation coordinate frame,  $\Sigma$ , as in Eq. (3) where the summation convention is implied.

$$\Sigma_{ij} = \mathbf{Q}_{ik} \mathbf{Q}_{jm} \sigma_{km} \quad (i, j, k, m = 1, 2, 3) \quad (3)$$

Similarly, the transformation of the coordinates from the cubic crystal coordinate frame to the sample frame is accomplished by the orthogonal matrix  $\mathbf{R}$  and its components are defined as  $\mathbf{R}_{ij} = \lambda_i \cdot \mathbf{E}_j$  where  $\lambda_i$  are the unit base vectors of cubic crystal frame in Fig. 4.

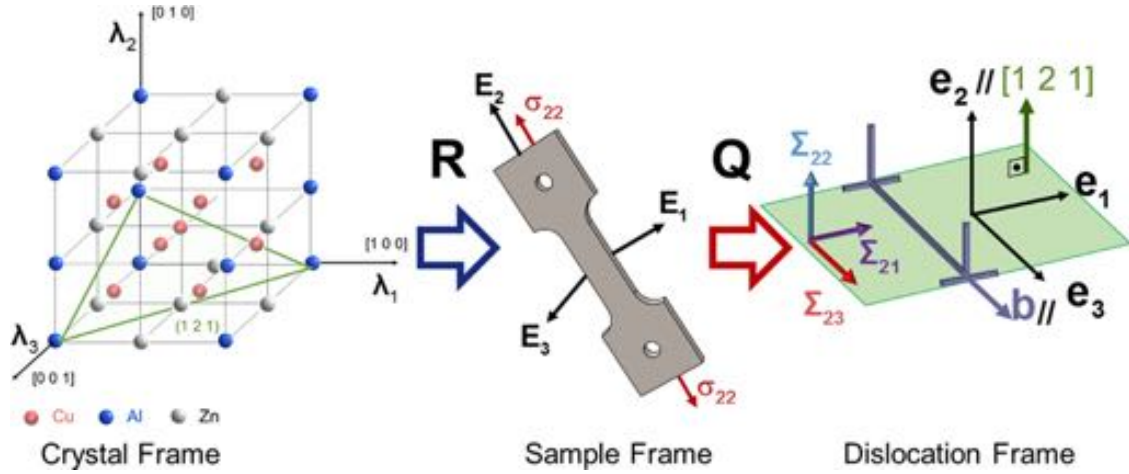


**Fig. 4.** Illustrates the cubic crystal frame [100]-[010]-[001], sample frame i.e.  $X_1 - X_2 - X_3$  (with the base vectors of  $\mathbf{e}_1 - \mathbf{e}_2 - \mathbf{e}_3$ ). As can be seen, the coordinate transformation matrices  $\mathbf{R}$  and  $\mathbf{Q}$  can be used to transform the corresponding coordinates between the cubic, the sample and the dislocation frames.

In order to establish a solution scheme,  $E_{tot}$ , is constructed explicitly as the equilibrium of the system corresponds to the minimum total energy configuration, i.e.  $\min. (E_{tot})$ , whether an external stress field is present or not. Following this step, we delineated an energy minimization algorithm to find the updated positions of the leading partial- core fractionals under increasing loading intensity. In this proposed scheme, CRSS level corresponds to the glide shear stress, i.e.  $\Sigma_{23}$ , beyond which the matrix of second order partial derivatives (Hessian matrix) of  $E_{tot}$  function has no positive eigenvalues with the prescribed constraint of positive fractional Burgers vectors.  $E_{tot}$  is composed of: (i) the individual line energies of the four partials:  $E_{line}$ , (ii) the interaction of the long-range elastic fields of these four partials:  $E_{int}$ , (iii) the misfit energies introduced due to the presence of NNAPB and NNNAPB faults:  $E_{mis}$  and (iv) the work done by the external stress field  $W$ .

$$E_{tot} = E_{line} + E_{int} + E_{mis} - W \quad (4)$$

The  $E_{line}$  term can be expressed as the sum of the individual line energies of four  $a/4$   $\langle 111 \rangle$  partials as follows:

$$E_{line} = E_{line,1} + E_{line,2} + E_{line,3} + E_{line,4} = E_{line,1} + \frac{3K_s b^2}{4\pi} \ln\left(\frac{R}{\xi}\right) \quad (5)$$

The variables  $R$  and  $\xi$  represent the outer cut-off and inner-cut off distances which are chosen as  $500b$  and half of the interplanar spacing,  $a'$ , across  $\langle 111 \rangle$  direction-complying with the original Peierls–Nabarro analysis, respectively. The slip initiation along  $\langle 111 \rangle$   $\{110\}$  or  $\langle 111 \rangle$   $\{112\}$  systems is associated with the glide of the leading partial; therefore, its individual line energy,  $E_{line,1}$ , is detailed in a fashion including the short-range energy contribution of the fractional dislocations composing the leading partial dislocation.

The long range interaction energy of the  $a/4$   $\langle 111 \rangle$  partials with each other,  $E_{int}$ , is expressed in Eq. (6) where  $p$  represents the number of the total partials, i.e. 4, and the separation distance between the third and fourth partials (the leading partial is denoted as the first partial), i.e.  $d_3$ , is taken as equal to  $d_1$  as shown in Fig. 2 (Wang and Sehitoglu, 2014):

$$E_{int} = \frac{K_s b^2}{4\pi} \left\{ \sum_{i=1}^{p-1} \left[ \sum_{j=1}^i \ln\left(\frac{R}{d_j}\right) + \sum_{j=2}^i \ln\left(\frac{R}{d_j}\right) + \sum_{j=3}^i \ln\left(\frac{R}{d_j}\right) \right] \right\} \quad (6)$$

The misfit energy created on the glide plane via creating stable NNAPB and NNNAPB fault ribbons spanning  $d_1$  and  $d_2$  distances in the dissociated configuration of a  $\langle 111 \rangle$  dislocation,  $E_{mis}$  is formulated as (2NNAPB and 1 NNNAPB type faults):

$$E_{mis} = 2\gamma_1 d_1 + \gamma_2 d_2 \quad (7)$$

Lastly, the energy contribution of the work done by the external stress,  $W$ , on the leading partial dislocation configuration is expressed in Eq. (8) as:

$$W = b_1 \tau_1 + b_2 \tau_2 + b_3 \tau_3 \quad (8)$$

where  $\{\tau_1, \tau_2, \tau_3\} = \{\Sigma_{23}, \Sigma_{23} \cos \omega - \Sigma_{13} \sin \omega, \Sigma_{23} \cos \alpha + \Sigma_{13} \sin \alpha\}$  following the coordinate transformation operations. It should be emphasized that as the CRSS level is determined based on the glide motion of the leading partial; the trailing partials do not contribute to the work expression in Eq. (8). The resolved components  $\{\tau_1, \tau_2, \tau_3\}$  are illustrated in Fig. 5 along with the non-planar structure of the leading partial core. It is to be noted that the conjugate plane angles,  $\alpha$  and  $\omega$ , are determined based on the geometry of the possible four core configurations A, B, C and D shown in Fig. 2.

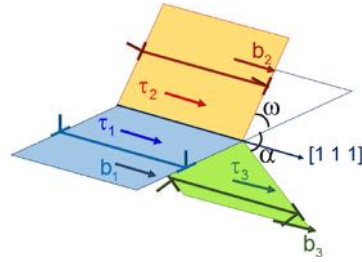


Fig. 5. Shows the geometry of the leading partial core and the resolved shear stresses  $\tau_1$ ,  $\tau_2$  and  $\tau_3$  acting on the core fractionals.

$E_{line,1}$ , is expressed in Eq. (9) as a combination of: (i) the line energies of the fractional dislocations posited inside the core,  $E_{fractional}$ , (ii) the interaction energies of these fractional dislocations,  $E_{inter-frac}$ , (iii) the misfit energy associated with the generalized stacking faults formed on the conjugate  $\{112\}$  and/or  $\{110\}$  planes:  $E_{fault}$ . It should be emphasized that the values of these energy terms are governed by the splitting configuration favored upon the minimization of  $E_{tot}$ .

$$E_{line,1} = E_{fractional} + E_{inter-frac} + E_{fault} = \sum_{j=1}^3 E_{fractional,j} + E_{inter-frac} + E_{fault} \quad (9)$$

The term  $E_{fractional}$  is comprised of the summation of the line energies associated with three fractional dislocations inside the leading partial and it is expressed as:

$$E_{fractional} = \sum_{i=1}^3 E_{fractional,i} = \frac{K_s}{4\pi} (b_1^2 + b_2^2 + b_3^2) \ln\left(\frac{R}{\xi}\right) \quad (10)$$

ensuring the conservation of the Burgers vector of the leading partial as expressed in Eq. (11):

$$\sum_{i=1}^3 b_i = b = |a/4 \langle 111 \rangle| \quad (11)$$

On the other hand, the interaction energy associated with the interplay of the elastic fields of these three core fractional dislocations are expressed as (Lejček and Kroupa, 1981):

$$E_{inter-frac} = \frac{K_{interaction}}{4\pi} \left( b_1 b_2 \ln \left[ \frac{R^2}{y_1^2 + y_2^2 + y_1 y_2} \right] + b_1 b_3 \ln \left[ \frac{R^2}{y_1^2 + y_3^2 + y_1 y_3} \right] + b_2 b_3 \ln \left[ \frac{R^2}{y_2^2 + y_3^2 + y_2 y_3} \right] \right) \quad (12)$$

A major point to emphasize is that the anisotropic elastic interaction coefficient  $K_{interaction} = 86.9$  GPa appearing in Eq. (12) is slightly different from  $K_s = 84$  GPa as the glide planes of the interacting fractional dislocations are not necessarily parallel and may exhibit different crystallographic symmetries along the directions normal to glide direction  $\langle 111 \rangle$  (Steeds, 1973; Lothe, 1992; Foreman, 1955) (The principal elastic stiffness tensor values of  $C_{11} = 116$  GPa,  $C_{12} = 102$  GPa and  $C_{44} = 84$  GPa (in Voigt notation) are employed).

In order to determine the misfit energy of the stacking faults inside the leading partial core separating the fractional dislocations, we need to introduce the mathematical expressions for the disregistry functions  $f_i(x_i)$  on the conjugate planes. The functions  $f_i(x_i)$  are the generalized forms of the  $u_x$  parameter in Fig. 1 which account for the spatial variation of the slip in defects particularly the localization effects in dislocations, and allow us to relate the GSFE value to the spatial coordinates  $x_i$  such that  $\gamma(u_x) = \gamma(f_i(x_i))$ . The non-planar disregistry distribution within the core region of the leading partial is described based on a general form initially proposed by Foreman et al. (1951) and Kroupa and Lejček (1972) which is expressed in Eq. (13).

$$f_i(x_i) = b_i + c_i \xi \left( \tan^{-1} \left( \frac{y_i - x_i}{\xi} \right) - \tan^{-1} \left( \frac{y_i}{\xi} \right) \right) (i = 1, 2, 3) \quad (13)$$

The parameters  $c_i$  are determined by the set of boundary conditions expressed in Eqs. (14) and (15). Among these two expressions, Eq. (14) indicates that the value of the disregistry functions  $f_i(x_i)$  correspond to the fractional Burgers vectors,  $b_i$ , at the dislocation line position  $x_i = 0$ . On the other hand, Eq. (15) implies that the localized slip present at the core center attenuates at far-field as  $x_i \rightarrow \infty$ .

$$f_i(0) = b_i \quad (14)$$

$$\lim_{x_i \rightarrow \infty} f_i(x_i) = 0 (i = 1, 2, 3) \quad (15)$$

By solving Eqs. (14) and (15) simultaneously, the  $c_i$  parameters are evaluated to be as:

$$c_i = \frac{b_i}{\xi \left[ \tan^{-1} \left( \frac{y_i}{\xi} \right) + \frac{\pi}{2} \right]} \quad (16)$$

Following the introduction of the disregistry function formalism, the misfit energy inside the leading partial core,  $E_{fault}$ , is expressed in a convergent serial form presented in Eq. (17) (Lothe, 1992; Tadmor and Miller, 2011):

$$E_{fault} = \sum_{i=1}^3 \sum_{m=-\infty}^{\infty} \gamma_i (f_i(ma' - y_i)) a' \quad (17)$$

In the expression of  $E_{fault}$ , the first summation on the right hand side is taken over the three conjugate planes on which the dislocation core spreads whereas the second sum represents the collection of the fault energy along each atomic row separated by a distance of  $a'$ . To that end, Eq. (17) accounts for the discrete structure of the lattice by expressing  $x_i$  coordinate as  $ma' - y_i$ . The equilibrium of the four  $a/4$   $\langle 111 \rangle$  partials under either zero or finite external stress necessitates the minimization of the total energy expression given in Eq. (4) which is detailed through Eqs. (5)–(17). This implies the determination of the Burgers vectors, i.e.  $b_1, b_2$  ( $b_3$  is given as  $b_3 = b - b_1 - b_2$ ) and the positions of the fractionals, i.e.  $y_1, y_2$  and  $y_3$ , inside the core region of the leading partial.

#### 2.4. Solution strategy

To solve for the positions of the fractionals  $\{y_1, y_2, y_3\}$  and the Burgers vectors  $\{b_1, b_2, b_3\}$ , we minimized  $E_{tot}$ :  $E_{tot}(y_1, y_2, y_3, b_1, b_2, b_3)$  via ensuring the equilibrium of fractional dislocations. The set of three equations which impose the equilibrium of the  $i^{\text{th}}$  fractional dislocation under external stress is written in Eq. (18) as follows:

$$\frac{\partial E_{tot}}{\partial y_i} = 0 \quad (i = 1, 2, 3) \quad (18)$$

Furthermore, the constraint presented in Eq. (11) imposes that the summation of the fractional Burgers vector should result into the leading partial Burgers vector,  $b$ , and results in 3 additional equations with an unknown Lagrange multiplier of  $\mu$  such that:

$$\nabla_{b_i} E_{tot} + \mu \nabla_{b_i} \left( \sum_{i=1}^3 b_i \right) = 0 \quad (19)$$

In Eq. (19),  $\nabla_{b_i}(\cdot)$  is the gradient operator with respect to the fractional Burgers vector  $b_i$ . Given the set of 7 equations in Eq. (11) and Eqs. (18)–(19), the set of 7 unknowns of  $\{y_1, y_2, y_3, b_1, b_2, b_3, \mu\}$  are solved numerically.

The expression of  $E_{tot}$  is denoted as “stable” up until the inactive constraints can be ensured in response to the proportional increase of  $\Sigma$  components. On the other hand, incremental loading physically tends to drive Burgers vectors of the fractional dislocations  $b_2$  and  $b_3$  into the unphysical negative sign domain and results in ill-conditioning (Fletcher, 2013). Therefore, the maximum value of glide stress  $\Sigma_{23}$  at which the presence of the local minimum of  $E_{tot}$  is ensured under the prescribed constraint corresponds to the CRSS level.

The solution strategy adopted herein differs from the minimization of the total energy functional proposed earlier for calculating the core configuration of  $a/2$   $\langle 111 \rangle$  dislocations in pure bcc metals (Vitek et al., 1972; Lejček, 1979). In that earlier approach,  $\rho_i(x_i)$  distributions on the conjugate planes are evaluated based on the integro-differential Peierls-Nabarro equation. In this work, the fractional dislocation concept is employed to transform the problem of energy functional minimization into a constrained minimization problem of differential calculus. The underlying reason for constructing a different strategy is that the interaction of the disregistry distributions on the conjugate planes introduces an irregular singularity. Unlike the weakly singular integral equations of which are known to be solved by iterative singular value decomposition techniques (Polyanin and Manzhirov, 2008), the existence of solutions for the non-linear, irregularly singular integro-differential equations within the presence of external stress tensor components is not guaranteed (Lejček, 1973). To that end, constraint minimization of  $E_{tot}$  is employed within the framework of the set of equations expressed in Eqs. (4)–(19).

### 3. Results

#### 3.1. A brief summary of the experimental results on CRSS in single crystals

The confluent effect of non-zero  $\Sigma$  tensor components on the dislocation glide resistance under uniaxial tensile and compression is presented in Fig. 6(a) from the experimental findings of Romero *et al.* at 323 K (Romero *et al.*, 1988). The glide resistance, CRSS, is quantified based on the critical value of  $\Sigma_{23}$  component. In order to configure the sample orientation and the uniaxial loading sense (either tensile or compressive) effects, the characteristic angle  $\chi$  of the maximum resolved shear stress plane (MRSSP) is utilized as shown in Fig. 6(b). In this representation convention, the angle  $\chi$  formed between MRSSP (the plane bearing highest resolved shear stress) and the  $\{110\}$  plane bearing the highest shear stress within the active  $\langle 111 \rangle$  slip zone, varies between  $-30^\circ$  and  $+30^\circ$ . It is to be emphasized that there is no geometrical restriction on MRSSP and it may coincide with any plane including the reference  $\{110\}$  plane. The sign of the angle  $\chi$  is taken as positive (negative) if the closest  $\{112\}$  plane to the MRSSP in the active  $\langle 111 \rangle$  slip zone is sheared along the anti-twinning (twinning) direction under tensile (compression) loading. This representation technique allows us to discern the single crystal orientation under uniaxial loading (Duesbery, 1984).

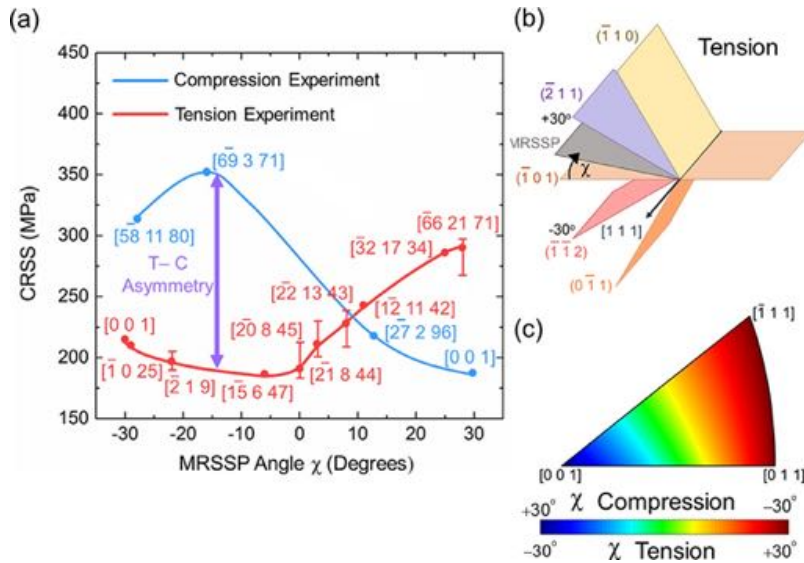


**Fig. 6.** (a) Shows the variation of the experimental CRSS values under uniaxial tension and compression at 323 K (Romero et al., 1988). It is to be noted that the abbreviation of “T-C” stands for “tension-compression”. (b) illustrates the geometrical interpretation of  $\chi$  angle for uniaxial tension. (c) shows the variation of  $\chi$  angle on the stereographic triangle for  $[111]$  slip direction under uniaxial tension and compression respectively. It is to be noted that in the convention employed, the  $\chi$  value is positive towards the uniaxial tension (compression) orientations favoring the shear along  $\langle 111 \rangle$   $\{112\}$  systems with in the active glide zone in anti-twinning (twinning) sense.

As can be seen in Fig. 6(a), the experimental CRSS levels do not correspond to a unique value and show significant variation ranging from 180 MPa up to 355 MPa under uniaxial tension and compression in response to the different single crystal orientations (Romero et al., 1988). The CRSS levels shown in Fig. 6 exhibit significant deviations from the Schmid Law reaching 95% relative difference between the different uniaxial loading orientations. This difference is fairly large and must be incorporated in any modelling efforts addressing the significant interplay between the core shape and the external stress tensor components.

Under tension, for  $\chi \leq 0^\circ$ , the glide is favored along the twinning sense on  $\{112\}$  glide planes as tabulated in Appendix A (Romero et al., 1988). On the other hand, slip traces are reported to coincide with the MRSSP and  $\{123\}$  planes following a wavy glide pattern for single crystal orientations with  $\chi > 0^\circ$  (Romero et al., 1988). The promotion of high index slip plane traces for the tensile orientations of  $\chi > 0^\circ$  is expected to be a consequence of the segmented slip of screw dislocations along the  $\{112\}$  and/or  $\{110\}$  planes which have been also observed in other bcc lattice structures such as in pure W (Marichal et al., 2013), Fe (Franciosi et al., 2015) and Fe-Si alloys (Šesták and Zárubová, 1965). On the other hand, this core fractional cross-glide phenomenon is not peculiar to the bcc-derivative lattices. A similar core transformation has been also imaged in a TEM study for the screw dislocations gliding on the prismatic and pyramidal planes intermittently in hcp structured Ti as a result of lattice friction differences in between these two planes (Clouet et al., 2015). In CuZnAl, the segmented, wavy glide for the tensile orientations of  $\chi > 0^\circ$  is expected to stem from the fact that the dislocations which are promoted to glide along the anti-twinning sense on  $\{112\}$  planes under external stress transform into a glissile configuration which is prone to slip along  $\langle 111 \rangle$   $\{110\}$  and  $\langle 111 \rangle$   $\{112\}$  twinning sense systems. The GSFE profile of  $\langle 111 \rangle$   $\{112\}$  anti-twinning glide system shown in Fig. 1 is expected to play a key role in this anomalous slip behavior.

For the single crystal orientations of  $\chi > 0^\circ$  under compression, slip initiates along the twinning sense of the  $\langle 111 \rangle$   $\{112\}$  systems and the high index slip planes are observed for the orientations of  $\chi < 0^\circ$ . The greatest CRSS differential between the uniaxial tension and the compression is observed within the range of  $\chi \in (-20^\circ, -10^\circ)$  and the tension-compression asymmetry vanishes within the close neighborhood of  $\chi \approx 10^\circ$ . As the change in the sign of  $\chi$  angle implies nothing but changing the sign of  $\Sigma$  components, this asymmetry in the CRSS values is surmised to be closely related to the different sessile to glissile transformation paths of the dislocation cores under external stress.

### 3.2. Sessile splitting of $a/4 \langle 111 \rangle$ leading partial core fractionals

The equilibrium core configuration of the screw character leading partial,  $a/4 [111]$ , in the absence of an external stress field is of significant importance as it constitutes an initial condition for the core shape evolution under external stress. To that end, we chose the four possible sessile core configurations shown in Fig. 2 in which the core fractionals split on different planes. Thereafter,  $E_{tot}$  is minimized to calculate the equilibrium configurations of the fractionals. Table 2, shows the corresponding Burgers vectors and the positions of the fractionals as well as  $E_{tot}$  values for each configuration shown in Fig. 7(a), (b), (c) and (d). As Table 2 and Fig. 7 suggest, the  $\{112\}$  planes sheared along the twinning sense in the  $\langle 111 \rangle$

**Table 2**

Tabulation of the maximum values of the disregistry distributions of  $f_i(x_i)$  ( $i=1,2,3$ ), namely the Burgers vector of each fractional split on either  $\{110\}$  or  $\{112\}$  conjugate planes, i.e.  $b_i$ , inside the core region of the leading  $a/4$   $[111]$  partial as well as the fractional positions,  $y_i$ , and the total energy values.

	Configuration A	Configuration B	Configuration C	Configuration D
$b_1$	0.62 b	0.38 b	0.44 b	0.52 b
$b_2$	0.13 b	0.31 b	0.24 b	0.18 b
$b_3$	0.25 b	0.31 b	0.32 b	0.30 b
$y_1$	1.56 b	1.20 b	1.38 b	1.22 b
$y_2$	0.60 b	1.05 b	0.98 b	0.84 b
$y_3$	0.25 b	1.05 b	1.16 b	1.06 b
$E_{tot}$ (nJ/m)	12.74	13.56	13.19	12.97

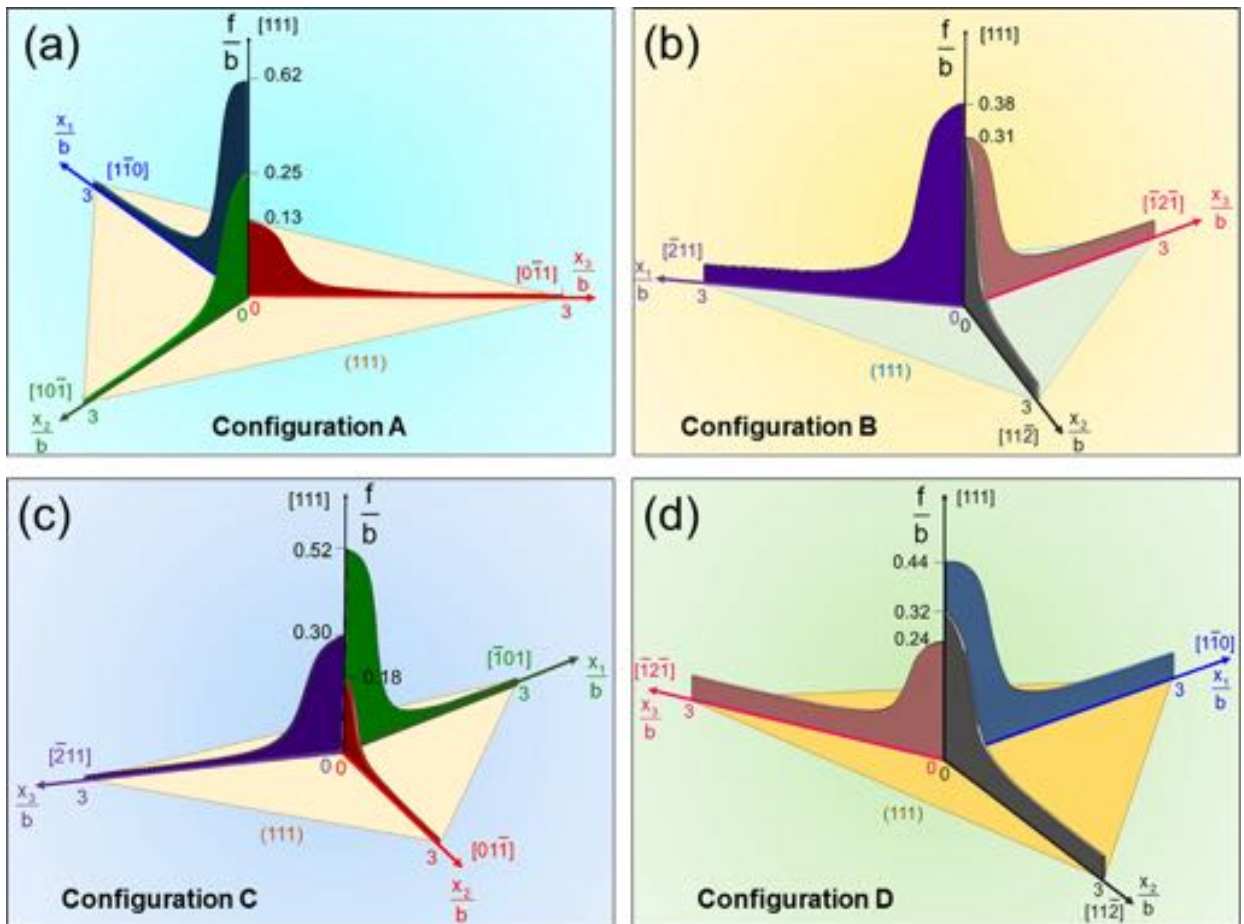


**Fig. 7.** Shows the sessile, externally stress-free core configurations which are grouped into four categories based on the number and the type of planes on which the fractionals are posited. (a) shows the leading core configuration split on only  $\{112\}$  planes, i.e. configuration A. (b) illustrates the sessile core split on  $\{110\}$  planes only, i.e. configuration B. (c) exhibits the core configuration in which fractionals split on two  $\{112\}$  planes and a single  $\{110\}$  plane, configuration C. In (d), the core fractionals prefer to split on a single  $\{112\}$  plane and two  $\{110\}$  planes, i.e. configuration D.

glide zone are energetically more favorable to bear greater Burgers vector in externally stress-free, sessile configuration. This behavior stems from the lower energy of the generalized stacking faults shearing these glide systems. Even though the slip geometries differ significantly for configurations A, B, C and D; only small variations are associated with the  $E_{tot}$  levels in the stress free configuration. Therefore, the external stress tensor can introduce transitions between the possible four configurations and hence can affect the resulting CRSS levels. This result necessitates a detailed consideration of the activation of all four configurations under external stress to accurately determine the corresponding CRSS levels.

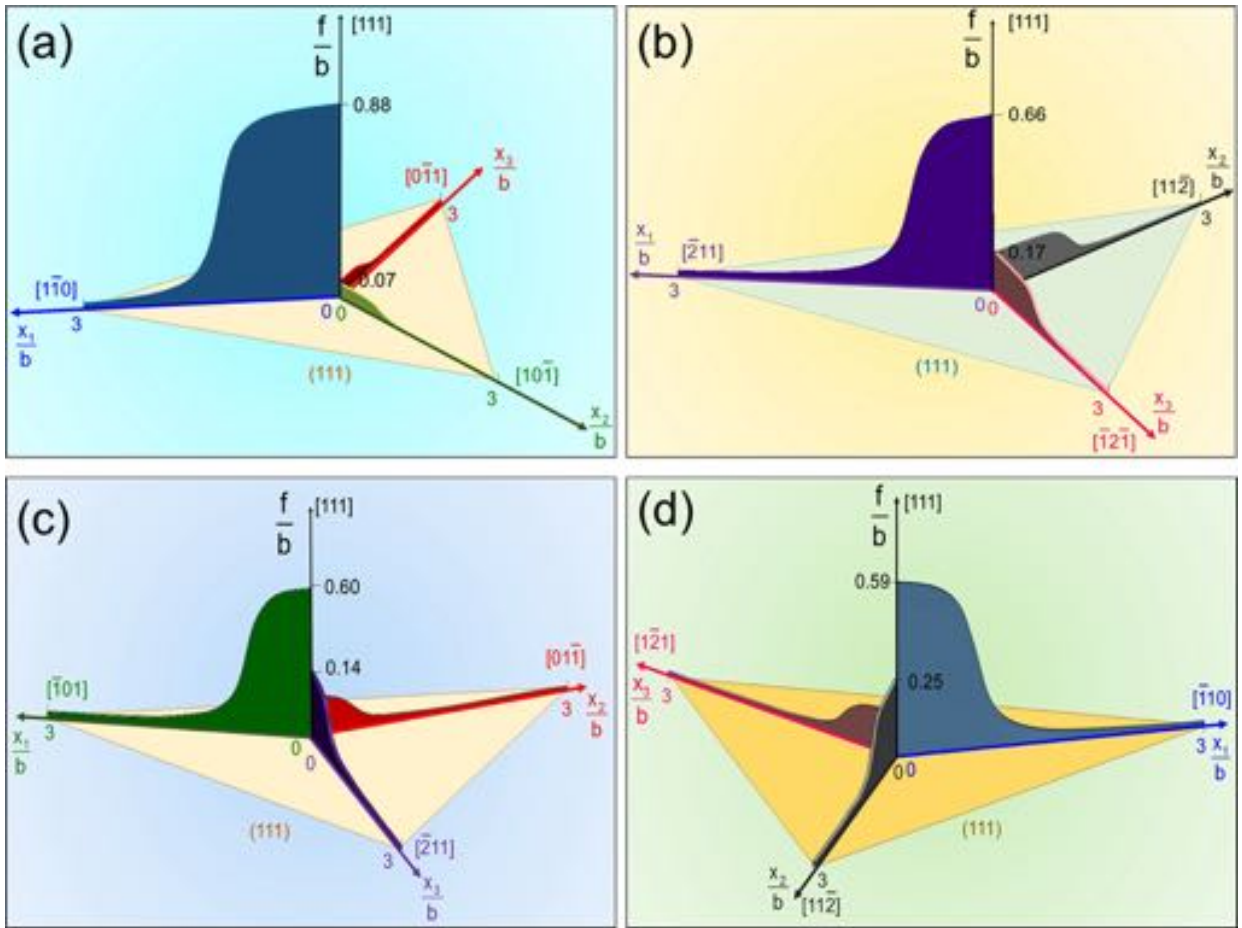


**Fig. 8.** Shows the theoretical variation of the disregistry distributions inside the non-planar core structure of  $a/4$   $[111]$  screw dislocation posited in a uniaxial tension specimen of  $E_1-E_2-E_3=[5\ 8\ 0]-[0\ 0\ 1]-[8\ 5\ 0]$  orientation. (a)–(d) shows the disregistry distributions evaluated based on the initial core configurations of A–B–C–D in Fig. 3. As can be seen the greatest disregistry distribution is observed for the configuration A on  $(\bar{1}\bar{1}2)[111]$  glide system complying with the experimentally reported active slip system (Romero et al., 1988).

### 3.3. The selective activation of configurations under uniaxial loading

In order to build an understanding on the effects of the loading orientation for the sessile to glissile core transformation, we evaluated the slip disregistry distribution of the leading  $a/4$   $[111]$  screw core for a sample oriented as  $E_1 - E_2 - E_3$  parallel to  $[5\ 8\ 0] - [0\ 0\ 1] - [8\ 5\ 0]$  triplet under uniaxial tensile loading parallel to  $E_2$ . Among the four possible configurations A, B, C and D shown in Fig. 2; the configuration A reaches the glissile shape earliest- at the lowest resolved shear stress magnitude, i.e. CRSS. The disregistry distribution inside these four core configurations at the instant of the glide initiation is shown in Fig. 8. As can be seen, complying with the fact that the core configuration A attains the glissile shape at the lowest CRSS level, the peak value of the normalized disregistry distribution on  $(\bar{1}\bar{1}2)[111]$  glide system, 0.88, is the greatest one among the other configurations (B, C and D), i.e. 0.66, 0.59 and 0.60 respectively. This result suggests that the re-distribution of disregistry inside the core under external stress may play a decisive role in the glide tendency of the leading partial. Furthermore, this trend in the glide resistance of the different configurations also complies with the experimentally observed glide behavior of the  $[001]$  tension sample in which the observed glide system is tabulated in Table A.2 (Romero et al., 1988).

This quantitative analysis suggests that the tendency of the non-planar screw core to attain a glissile shape should be assessed with the transferability of the slip to a favorable glide system from the other conjugate planes that the core extends on. The transfer of slip inside the core region casts the core in a nearly planar shape decreasing the CRSS level. This attitude in the core structure complies with the original Peierls-Nabarro model suggesting a lower glide resistance for a wider planar core (Lothe, 1982). Quantitative evidence between the glide tendency and the planarity of the core structure has been also observed for NiTi within the framework of atomistic scale simulations in our previous work (Alkan and Sehitoglu, 2017). The active configurations simulated for the other loading orientations are also tabulated in Appendix A. The variation of the core planarity and the active core configuration under varying uniaxial loading orientation suggests that the external

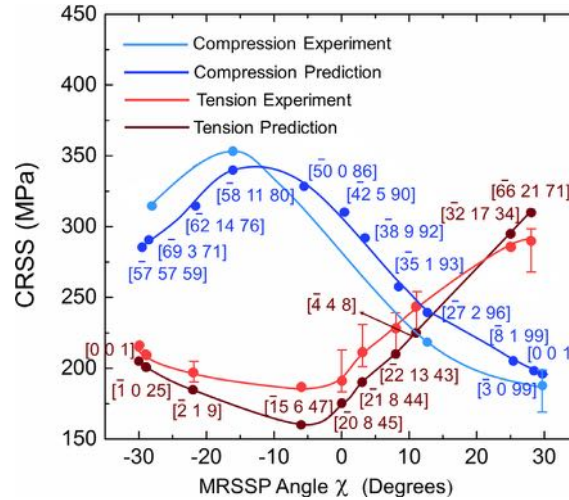


**Fig. 9.** Shows the theoretical CRSS values within range of  $\chi = -30^\circ$  and  $+30^\circ$  under uniaxial tension and compression. The experimental CRSS measurements of Romero et al. (1988) (at 323 K) are also included for comparison purposes.

stress tensor governs on the core splitting geometry; and therefore, on the CRSS level. This correspondence between the core shape and the CRSS level will be detailed in the following section.

### 3.4. Theoretical predictions of CRSS under uniaxial tension and compression

Following the formulation introduced in Sections 2.3 and 2.4, we evaluated the theoretical critical glide stress values, i.e. theoretical CRSS, and plotted them in Fig. 9 in comparison with the uniaxial tension and compression experiments of Romero et al. (1988). As can be seen, the theoretical predictions can capture the trend observed in the experimental measurements in a reasonably well agreement. This close trend between the theory and the experiments allows us to deduce the possible underlying mechanisms for the non-Schmid behavior in CRSS values of CuZnAl. Tension-compression asymmetry shown in Fig. 9 exhibits strong anisotropy. Meanwhile, the CRSS differentials extend up to 175 MPa for the set of orientations  $\chi \in (-15^\circ, -5^\circ)$ , it almost vanishes for  $\chi \in (10^\circ, 15^\circ)$  interval. Activation of the distinct slip systems in these crystallographic orientations provides evidence for the presence of a direct link with the core shape and the corresponding CRSS levels. In order to shed light on the interplay between the core shape and the CRSS levels, we plotted the theoretical distribution of core disregistry displacements for the  $[\bar{5}8\ 11\ 80]$  compression, the  $[\bar{1}5\ 6\ 47]$  tension, the  $[\bar{2}7\ 2\ 96]$  compression and the  $[\bar{4}4\ 8]$  tension samples respectively in Fig. 10(a)–(d) at the instant of  $\Sigma_{23} = \text{CRSS}$ .

A close examination of Fig. 10(a) and (b) demonstrates that the planarity of the disregistry distribution inside the leading partial core spreading plays a key role in the major CRSS differential plotted in Fig. 9 between the  $[\bar{5}8\ 11\ 80]$  compression and the  $[\bar{1}5\ 6\ 47]$  tension samples. The core shape preserves its non-planarity for the  $[\bar{5}8\ 11\ 80]$  compression sample as the glide shear stress reaches the CRSS value, as shown in Fig. 10(a). On the contrary, the planarity of the core structure can be clearly observed in the  $[\bar{1}5\ 6\ 47]$  tension sample in which the core disregistry is concentrated mostly on the  $(\bar{1}\bar{1}2)$  glide plane, with a Burgers vector of  $b_1 = 0.94\ b$  in Fig. 10(b). These theoretical disregistry distributions suggest that the planar core structures can decrease the corresponding CRSS levels compared to the non-planar core spreading. This core planarity effect is evaluated to result in strong anisotropy in the glide resistance of CuZnAl depending on the sample orientation.

But not all of the sample orientations suffer from the strong CRSS asymmetry between the uniaxial tension and compression. As can be seen in Fig. 9, within the range of  $\chi$  values of  $(10^\circ, 15^\circ)$ , the gap between the CRSS values are almost indistinguishable. On theoretical grounds, this behavior stems from the very similar core shape attained under external stress as exemplified for the  $[\bar{4}4\ 8]$  tension and the  $[\bar{2}7\ 2\ 96]$  compression samples as shown in Fig. 10(c) and (d) at the instant of  $\Sigma_{23} = \text{CRSS}$ . The minor differences in these two core spreading cases are surmised to stem from the distinct GSFE profiles of the  $\langle 111 \rangle$   $\{110\}$  and  $\langle 111 \rangle$   $\{112\}$  systems.

These illustrative cases clearly suggest that the promoted core configuration and the corresponding disregistry profiles are in close relationship with the CRSS values measured/calculated. The planarity of the core structure facilitates glide motion and plays a key role in the anisotropic behavior of CRSS levels. The instability of the  $E_{tot}$  expression to pinpoint the glide initiation is shown to result in close agreement with the experimental behavior in CuZnAl. On the other hand, this method requires a case by case examination and should be further extended into an applicative form to be employed in continuum scale crystal plasticity calculations. In the following section, this point will be addressed with a proposed generalized yield criterion.

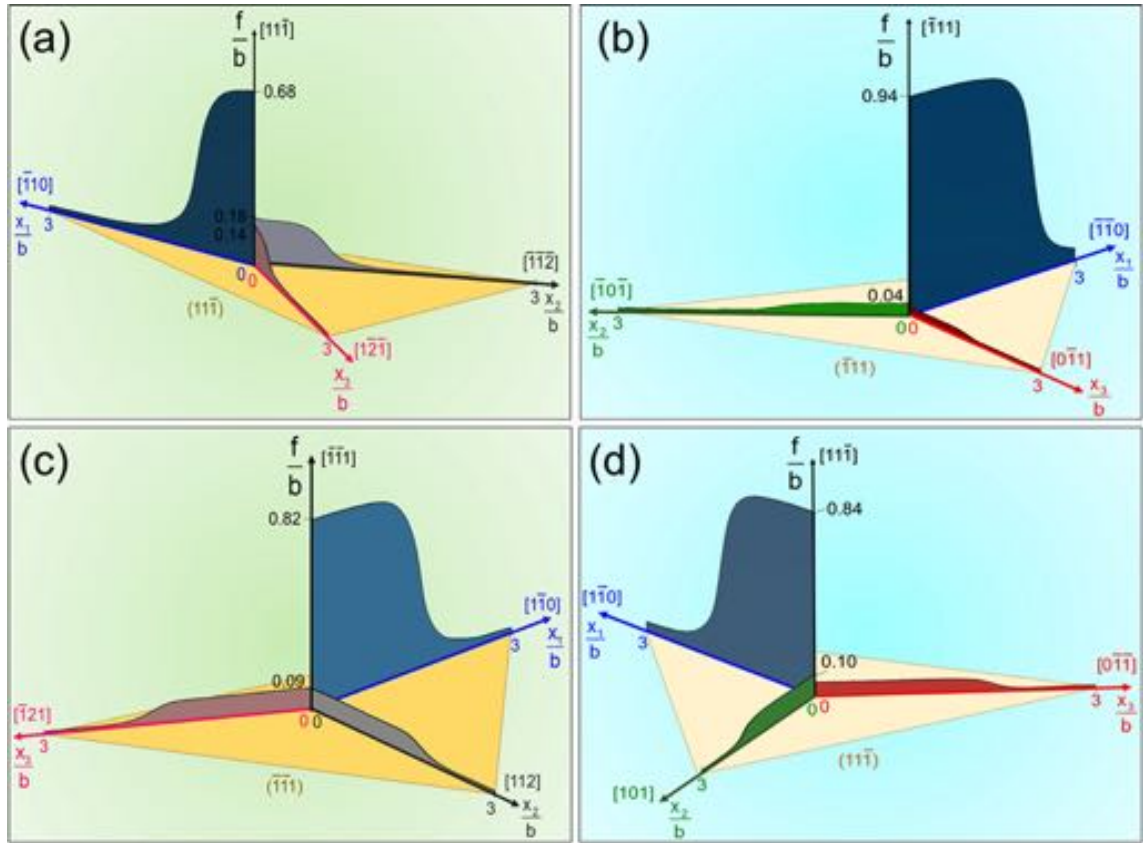


**Fig. 10.** (a) shows the disregistry distribution inside the leading partial core evaluated for the  $[\bar{5}8\ 11\ 80]$  sample under uniaxial compression at the instant of glide initiation. Similarly, (b) shows the disregistry distribution evaluated for the  $[\bar{1}5\ 6\ 47]$  sample under uniaxial tension. As can be seen by comparing the core configurations shown in (a) and (b), the transferability of the non-planar disregistry distribution into a planar shape is of paramount importance governing on the experimental and the theoretical CRSS values plotted in Fig. 9. The non-planar core shape of the leading partial posited in the  $[\bar{5}8\ 11\ 80]$  compression sample introduces an increase of 175 MPa in the CRSS level compared to the  $[\bar{1}5\ 6\ 47]$  tension sample which is in line with the experimental 165 MPa difference. On the other hand, the CRSS values are very close, by only 10 MPa, for the  $[\bar{4}\ 4\ 8]$  tension and the  $[\bar{2}7\ 2\ 96]$  compression samples of which the core disregistry distributions at the instant of glide initiation are plotted in (c) and (d), respectively. As can be seen in (c) and (d), the disregistry distributions are very similar for both samples. The underlying reason for the minor difference in CRSS levels can be attributed to the GSFE profiles of  $\{111\}$   $\{110\}$  and  $\{112\}$  planes which contribute to  $E_{tot}$  as manifested in a detailed fashion in *Methods and Theoretical Background* section.

### 3.5. Construction of a yield surface for the generalized stress states

Following the theoretical efforts in modelling the anisotropic glide behavior of CuZnAl in the previous sections; we established a compact, analytical yield criterion as a function of the theoretical external stress tensor components at the instant of plastic flow. Broadly speaking, this approach allows to generate a closed form expression serving as a quantitative tool for identifying the slip initiation in CuZnAl alloy within the framework of a macroscale crystal plasticity perspective. To accomplish this task, we incorporated the independent deviatoric stress tensor components  $S_{ij}$  ( $i, j = 1, 2, 3$ ) which are defined as  $S_{ij} = \Sigma_{ij} - 1/3\text{trace}(\Sigma)\delta_{ij}$  ( $\delta_{ij}$ : Kronecker Delta), into a linear expression presented in Eq. (20). The coefficients  $\tau_{cr}$  and  $a_i$  ( $i = 1, 2, 3, 4$ ) are evaluated by multi-linear regression of the theoretical deviatoric stress components from the energy minimization calculations at the instant of plastic slip initiation such that  $S_{23} = CRSS$ . The resulting yield surface is plotted in Fig. 11.

$$\tau_{cr} = S_{23} + a_1 S_{21} + a_2 S_{11} + a_3 S_{22} + a_4 S_{13} \quad (20)$$

**Table 3**

Tabulation of the coefficients generating the generalized yield surface plotted in Fig. 11, i.e.  $\tau_{cr}$ ,  $a_1$ ,  $a_2$ ,  $a_3$  and  $a_4$ . The coefficients are evaluated based on multi-variable regression of the theoretical deviatoric stress components at the instant of glide initiation at which  $\Sigma_{23} = S_{23} = CRSS$ .

	$\tau_{cr}$	$a_1$	$a_2$	$a_3$	$a_4$
260	0.85	0.71	0.56	0.25	

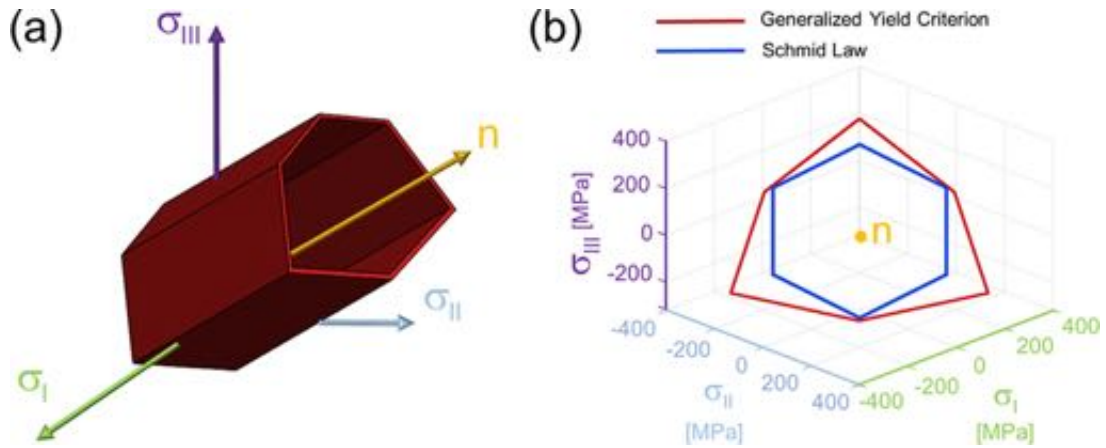


**Fig. 11.** (a) illustrates the predicted yield hypersurface in the principal stress space. Complying with the previous studies (Alkan et al., 2017; Hill, 1998), the predicted yield surface is of cylindrical topology with a symmetry axis of  $n = \Gamma[1, 1, 1]$ . (b) shows the yield surface projection on the  $\pi$  plane which is normal to  $\mathbf{n}$  vector. As can be seen, significant asymmetry is present in the generalized yield surface suggesting the major deviations from the conventional Schmid Law.

In order to visualize the resulting effect of the deviatoric stress components other than the glide shear stress  $\Sigma_{23}$  ( $= S_{23}$ ); the external stress state tensor is expressed in principal stress space of  $\sigma_I - \sigma_{II} - \sigma_{III}$  in a diagonalized form. Following this step, the principal stress components are parameterized utilizing two characteristic angles of  $\theta$  and  $\phi$  as well as the proportionality constant  $\lambda$ . In this mathematical representation scheme,  $\theta$  is the angle between the principal stress vector  $\mathbf{T} = [\sigma_I, \sigma_{II}, \sigma_{III}]$  and  $\sigma_I = [\sigma_I, 0, 0]$ ; where as  $\phi$  stands for the angle between projection of  $\mathbf{T} = [\sigma_I, \sigma_{II}, \sigma_{III}]$  onto the  $\sigma_{III} = [0, 0, \sigma_{III}]$  plane and the  $\sigma_I = [\sigma_I, 0, 0]$  vector. The magnitude of the proportionality constant  $\lambda$  depends on the minimum resolved glide shear stress component acting on the possible glide systems satisfying the generalized yield criterion given in Eq. (20).

To calculate the CRSS levels and the associated deviatoric stress tensor components, we discretized the definition range of  $\theta$  and  $\phi$ , i.e.  $\theta = [0, \pi]$  and  $\phi = [0, 2\pi]$ , into 100 increments. Thereafter, the resulting yield hypersurface is generated in the principal stress space in Fig. 11(a) along with its projection onto the deviatoric plane - also denoted as  $\pi$  plane- in Fig. 11(b). It should be noted that  $\mathbf{n} = \Gamma[1, 1, 1]$  where  $\Gamma = 1/3(\sigma_I + \sigma_{II} + \sigma_{III})$ .

#### 4. Discussions

The solution of the total energy function encompassing the dislocation core spreading on  $\{112\}$  and  $\{011\}$  planes has enabled us to configure the core shapes with the corresponding disregistry functions under external stress without a priori assumptions. The dislocation configurations that are energetically most favorable were identified on a case by case basis. This methodology allowed determination of CRSS levels associated with slip in tension and compression. The resulting CRSS levels plotted as a function of loading orientation exhibit dramatic variations in their magnitudes and show close agreement with the experiments (Romero et al., 1988). The results point to much higher CRSS levels under uniaxial compression compared to tension that can partly explain the wider superelasticity temperature range observed in compression compared to tension (Wu et al., 2017). Considering that the transformation stresses are far below 25 MPa (Wu et al., 2017); the CRSS levels exceeding 180 MPa can result in long term performance as the higher slip resistance is known to improve functionality of shape memory alloys (Chowdhury and Sehitoglu, 2017). The overall non-Schmid effects in CuZnAl (CRSS variation from 180 MPa to 355 MPa) are much higher than the NiTi case pointing to the presence of the strong plastic anisotropy effects complying with the high Zener anisotropy ratio of 12 (Verlinden et al., 1984). The major deviations from the Schmid Law may result in high internal stresses and be responsible for the complex constitutive response in these alloys including hysteresis and the texture effects.

Accommodation of plastic deformation is mainly accomplished by the a  $\langle 111 \rangle$  screw character dislocations on  $\{112\}$  and  $\{110\}$  glide planes in  $L2_1$  ordered CuZnAl although the presence of quenching induced sessile dislocations on the  $\langle 001 \rangle$   $\{110\}$  system has been also reported (Lovey and Torra, 1999). The evolution of the leading partial core configurations from a sessile to a glissile shape under external stress are evaluated within the framework of the energetic arguments and the variation of the core spreading has been demonstrated to play a decisive role in the anisotropic glide resistance of CuZnAl. The calculated core configurations suggest that core planarity facilitates the glide motion leading to the lower CRSS levels. Furthermore, the resulting CRSS values are forwarded to establish a generalized yield criterion along with the external stress tensor components. To that end, the determination of atomistically informed CRSS levels under external stress tensor presents itself as a prospective quantitative tool for the macroscale crystal plasticity calculations nurturing strong ties with the core configurations.

It is to be noted that the original Peierls-Nabarro treatment has proved itself successful in capturing the anisotropic trend in CRSS levels. On the other hand, the resulting predictions are usually 3 to 4 times greater in magnitude than the experimental measurements. In this work, by varying both short and long range energy terms as a function of applied stress state embracing the non-planar core geometry, CRSS predictions are demonstrated to be in excellent agreement with the experimental measurements. On the other hand, the contribution of thermally activated mechanisms to CRSS levels at finite temperatures should be necessarily recognized to assess the limits of the current analysis (Taylor, 1992).

The contribution of a  $\langle 111 \rangle$  screw dislocations in the plastic deformation of CuZnAl is not limited to the austenitic phase. CuZnAl can go into thermally/stress-induced thermoelastic martensitic transformation from the austenitic  $\beta$  phase ( $L2_1$  ordered) to the martensitic 18R phase. To that end, the inherited a  $\langle 111 \rangle$  dislocations from the austenite phase can also prevail on the functional behavior of CuZnAl. Following the phenomenological theory of martensitic transformation (Wechsler et al., 1953; De Vos et al., 1978), it is shown in Appendix B that  $\langle 111 \rangle \{110\}$  and  $\langle 111 \rangle \{112\}$  glide directions of austenite phase are inherited as  $\langle 120 \rangle_{18R} \{22\ 11\ 2\}_{18R}$  and  $\langle 120 \rangle_{18R} \{211\}_{18R}$  into the 18R martensite phase. The inherited dislocations in the 18 R phase are not as glissile as they are in the austenitic phase as shown in Fig. B.2 and discussed in Appendix B regarding the magnitude of the resolved glide stress acting on them. In response, these inherited defects may introduce internal stresses affecting both forward and the reverse transformation behavior [Chowdhury and Sehitoglu, 2016; Romero and Ahlers, 1989; Sade et al., 2007]. The resulting internal stress fields may widen the hysteresis and increase the critical forward transformation stress stabilizing the austenitic  $\beta$  phase (Lovey and Torra, 1999). Furthermore, the stress fields around the dislocations may even promote the nucleation of preferential variants. The core configuration of partial dislocations and the deviations from Schmid Law is of paramount importance in describing the interplay between the austenitic slip and martensitic transformation. On the other hand, a thorough explanation of these intrigue interaction mechanisms necessitates to build a profound quantitative knowledge regarding the plastic slip and martensitic transformation mechanisms in CuZnAl. Therefore, this work aims to shed light on the theoretical characterization of slip initiation in the austenitic CuZnAl within the framework of slip energetics formulation. In fine, the resulting CRSS values are shown to exhibit strong deviations from the Schmid Law as a function of the core configurations promoted under external stress. Theoretical calculations exhibit close agreement with the experimental measurements and pave the way for establishing a generalized yield criterion for macroscale crystal plasticity modelling efforts.

It should be noted that the magnitude of the observed asymmetry between the different single crystal orientations establishes a motivation to comprehend the functional performance of polycrystalline CuZnAl (Gall et al., 1998). Since drawn CuZnAl has evidence of crystallographic texture, it is extremely important to understand the anisotropic variations in the CRSS levels. The current methodologies for describing the flow behavior of the Cu based shape memory alloys are rather simple, and do not recognize the important role of anisotropic slip resistance in shape memory behavior. To that end, the resultant generalized yield criterion should assist those researchers who are modeling plasticity of Cu-based shape memory alloys at the continuum level.

## 5. Conclusions

Following conclusions are drawn from this work:

- (1) The orientation dependence of slip stress in CuZnAl is significant and shows a complex trend due to the activation of  $\langle 111 \rangle \{112\}$  and  $\langle 111 \rangle \{011\}$  systems depending on the orientation.
- (2) The difference in the generalized stacking fault energy curves of  $\{112\}$  plane along the twinning and the anti-twinning senses can not solely explain the large orientation dependence of the CRSS levels in CuZnAl. Appreciation of the CRSS levels which deviate from the Schmid Law, necessitates to interrogate the core configurations in detail.
- (3) The results point that the non-planar core structures spread on conjugate  $\{112\}$  and  $\{011\}$  planes are categorized into four distinct fractional dislocation combinations which minimizes the overall energy. The calculations utilizing the dislocation core configurations produce the correct experimental trends in CRSS.
- (4) The results show that the planarity of the disregistry distributions inside the leading partial core plays a significant role in the magnitude of the CRSS levels. The planar core structures are demonstrated to facilitate the glide motion.
- (5) The proposed generalized yield criterion exhibits significant departure from the Schmid Law, and demonstrates the complexity of the slip anisotropy observed in shape memory alloys.

## Acknowledgments

The work is supported by Nyquist Chair funds.

## Appendix A

The crystallographic orientations of the simulated samples under uniaxial tension and compression are tabulated in Table A.1 for the uniaxial compression and Table A.2 for the uniaxial tension based on the experimental data reported for CuZnAl at 323 K in Romero et al. (1988). Furthermore, the active leading partial core configurations calculated within the framework of  $E_{tot}$  expression developed in Methods and Theoretical Background are also included.

**Table A.1**

The characteristic angle  $\chi$ , the crystallographic directions parallel to the sample frame base vectors  $\mathbf{E}_1$ – $\mathbf{E}_2$  and the dislocation frame base vectors  $\mathbf{e}_2$  –  $\mathbf{e}_3$  are tabulated for the uniaxial compression loading acting in line with  $\mathbf{E}_2$  along with the favored configuration, i.e. either A, B, C or D.

$\chi$	Uniaxial compression		Active configuration
	$\mathbf{E}_1$ – $\mathbf{E}_2$	$\mathbf{e}_2$ – $\mathbf{e}_3$	
–29.7°	[1 1 0]–[ $\bar{5}$ 7 57 59]	[123]–[ $\bar{1}$ 1 $\bar{1}$ ]	D
–28.7°	[1 23 0]–[ $\bar{6}$ 9 3 71]	[1 $\bar{2}$ 3]–[ $\bar{1}$ 11]	C
–21.54°	[0 38 $\bar{7}$ ]–[ $\bar{6}$ 2 14 76]	[1 $\bar{2}$ 3]–[ $\bar{1}$ 1 $\bar{1}$ ]	C
–16.26°	[11 58 0]–[ $\bar{5}$ 8 11 80]	[123]–[11 $\bar{1}$ ]	D
–6.11°	[43 0 25]–[ $\bar{5}$ 0 0 86]	[011]–[11 $\bar{1}$ ]	B
0°	[0 18 1]–[42 5 90]	[1 $\bar{2}$ 1]–[ $\bar{1}$ 11]	A
3.13°	[3 19 0]–[ $\bar{3}$ 8 6 92]	[1 $\bar{2}$ 1]–[ $\bar{1}$ 11]	A
7.61°	[1 35 0]–[ $\bar{3}$ 5 1 93]	[1 $\bar{2}$ 1]–[ $\bar{1}$ 11]	A
12.68°	[2 27 0]–[ $\bar{2}$ 7 2 96]	[1 $\bar{2}$ 1]–[11 $\bar{1}$ ]	A
25.02°	[1 8 0]–[ $\bar{8}$ 1 99]	[1 $\bar{2}$ 1]–[11 $\bar{1}$ ]	A
28.3°	[33 0 1]–[ $\bar{3}$ 0 99]	[ $\bar{1}$ 2 $\bar{1}$ ]–[111]	A
30°	[0 1 0]–[0 0 1]	[ $\bar{2}$ 11]–[ $\bar{1}$ 1 $\bar{1}$ ]	A

**Table A.2**

The characteristic angle  $\chi$ , the crystallographic directions parallel to the sample frame base vectors  $\mathbf{E}_1$ – $\mathbf{E}_2$  and the dislocation frame base vectors  $\mathbf{e}_2$  –  $\mathbf{e}_3$  are tabulated for the uniaxial tension loading acting in line with  $\mathbf{E}_2$  along with the favored configuration, i.e. either A, B, C or D.

$\chi$	Uniaxial tension		Active configuration
	$\mathbf{E}_1$ – $\mathbf{E}_2$	$\mathbf{e}_2$ – $\mathbf{e}_3$	
–30°	[5 8 0]–[0 0 1]	[ $\bar{1}$ 1 $\bar{2}$ ]–[1 1 1]	A
–28.6°	[7 3 0]–[ $\bar{1}$ 025]	[1 1 2]–[ $\bar{1}$ 11]	A
–22.43°	[9 1 1]–[ $\bar{2}$ 1 9]	[1 $\bar{1}$ 2]–[ $\bar{1}$ 11]	A
–5.52°	[2 5 0]–[ $\bar{1}$ 5 6 47]	[1 $\bar{1}$ 2]–[ $\bar{1}$ 11]	A
–0.15°	[2 5 0]–[ $\bar{2}$ 0 84 5]	[1 $\bar{1}$ 2]–[ $\bar{1}$ 11]	A
2.93°	[0 $\bar{1}$ 1 2]–[ $\bar{2}$ 1 8 44]	[011]–[ $\bar{1}$ 11]	B
7.71°	[0 $\bar{4}$ 3 13]–[ $\bar{2}$ 2 13 43]	[011]–[ $\bar{1}$ 11]	B
10.89°	[1 1 0]–[4 4 8]	[ $\bar{1}$ 32]–[ $\bar{1}$ 11]	D
25.12°	[02 $\bar{1}$ ]–[ $\bar{3}$ 2 17 34]	[ $\bar{1}$ 32]–[ $\bar{1}$ 11]	D
27.81°	[7 22 0]–[ $\bar{6}$ 6 21 71]	[ $\bar{1}$ 32]–[ $\bar{1}$ 11]	D

## Appendix B

To develop a solid understanding for the contribution of the austenitic-inherited slip on the pseudoelastic behavior of CuZnAl, the crystallographic aspects of the martensitic transformation from  $L2_1$  to 18R crystal structure should be revisited. To that end, following the generalized crystallographic theory of martensitic transformation of Wechsler et al. (1953) (WLR theory) from bcc to 18R crystal structures, the glide planes and the directions inherited from the austenite phase into the martensitic phase are derived.

In order to accomplish this task, firstly, the lattice correspondence between the austenitic  $L2_1$  structure ( $\beta$  phase) and the martensitic 18 R structure ( $\beta'$  phase) is introduced as De Vos et al. (1978) (no subscript is employed for the  $\beta$  phase indices throughout the text):

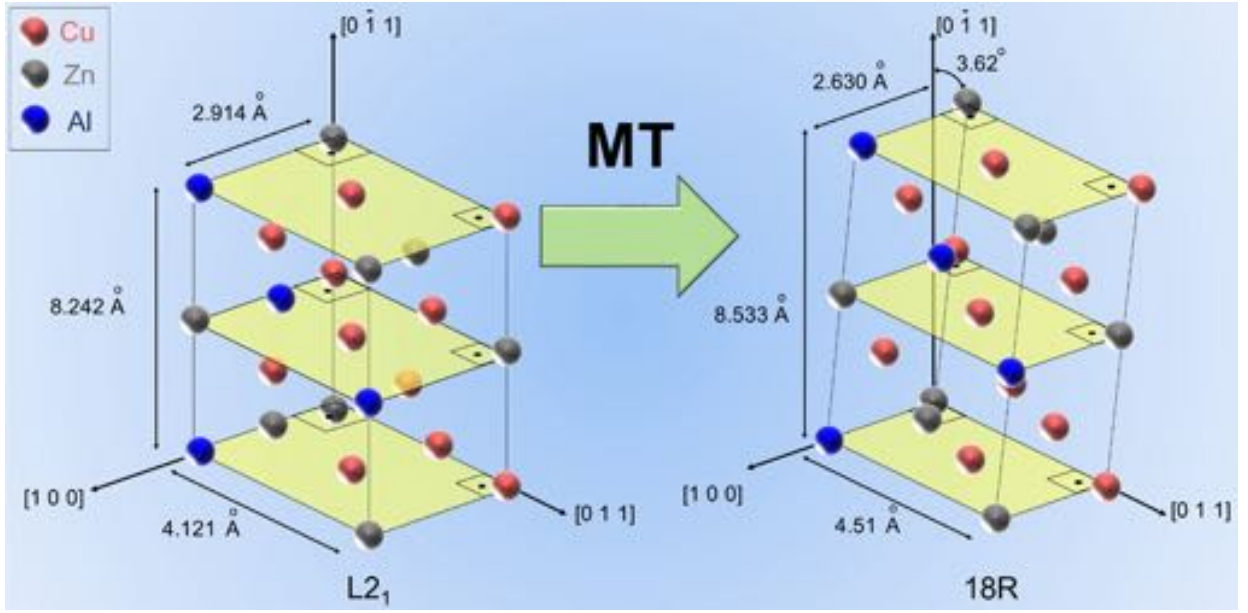
$$[100]_{18R} // [100] \quad [010]_{18R} // [011] \quad [001]_{18R} // [0\bar{1}1] \quad (B.1)$$

Table B.1 summarizes the lattice parameters of  $L2_1$  and 18 R structures (shown in Fig. B.1) evaluated from the ab-initio simulations (Wu et al., 2015).

**Table B.1**

Tabulation of the lattice parameters for  $L2_1$  and 18R structures evaluated from the ab-initio calculations (Wu et al., 2015).

$L2_1$		18R	
A	$a_{18R}$	$b_{18R}$	$c_{18R}$
5.828 Å	5.26 Å	4.51 Å	38.4 Å



**Fig. B.1.** This figure illustrates the lattice structures in  $L2_1$  ordered austenitic phase and 18 R structured martensite phase under the combined action of  $\mathbf{M}$  and  $\mathbf{T}$  deformation tensors.

**Table B.2**

Tabulation of values of the parameters  $\eta_1$ ,  $\eta_2, \eta_3$  and  $g$ , based on the lattice constants and the electron microscopy measurements of [de Vos et al. \(1978\)](#).

$\eta_1$	$\eta_2$	$\eta_3$	$g$
0.911	1.0681	1.5034	0.1568

Thereafter, following the WLR theory, the total deformation gradient tensor,  $\mathbf{F}$ , is expressed as in Eq. (B.2):

$$\mathbf{F} = \mathbf{RMT} \quad (\text{B.2})$$

where  $\mathbf{R}$ ,  $\mathbf{M}$  and  $\mathbf{T}$  are the rotation, the lattice invariant shear and the homogeneous lattice deformation tensors. These tensors are explicitly given as:

$$\mathbf{R} = \frac{1}{\eta_1 + \eta_2\eta_3} \begin{bmatrix} 1 + \eta_1\eta_2\eta_3 & \eta_3(\eta_1^2 - 1)(\eta_2^2 - 1) & (\eta_3^2 - 1)(1 - \eta_1^2) \\ (1 - \eta_1^2)(\eta_2^2 - 1) & \eta_1\eta_2 + \eta_3 & (\eta_2^2 - 1)(\eta_3^2 - 1) \\ \eta_2(\eta_3^2 - 1)(\eta_1^2 - 1) & \eta_1(1 - \eta_2^2)(\eta_3^2 - 1) & \eta_2 + \eta_1\eta_3 \end{bmatrix} \quad (\text{B.3})$$

$$\mathbf{M} = \begin{bmatrix} 1 & 0 & 0 \\ 0 & 1 & g \\ 0 & 0 & 1 \end{bmatrix} \quad (\text{B.4})$$

$$\mathbf{T} = \begin{bmatrix} \eta_1 & 0 & 0 \\ 0 & \eta_2 & 0 \\ 0 & 0 & \eta_3 \end{bmatrix} \quad (\text{B.5})$$

With this given structure,  $\mathbf{F}$  is an homogeneous deformation tensor and maps vectors into vectors and planes into planes ([Wechsler et al., 1953](#)). It is to be noted that there are two existing solutions for the lattice invariant shear,  $g$ , appearing in Eq. (B.4), within the context of invariant plane deformation, i.e. denoted as  $g_1$  and  $g_2$  ([De Vos et al., 1978](#)). These shears are evaluated in terms of,  $\eta_2$  and  $\eta_3$  as:

$$g_{1,2} = \pm \frac{1}{\eta_3} \sqrt{(\eta_2 - 1)^2 (\eta_3 - 1)^2} \quad (\text{B.6})$$

For demonstration purposes, only the minimum magnitude of these two shears,  $g = \min(|g_1|, |g_2|)$ , will be employed in the following analysis. On the other hand, it should be emphasized that the conclusions deduced are analogous for both cases on physical grounds. [Table B.2](#) tabulates the values of the parameters  $\eta_1$ ,  $\eta_2$ ,  $\eta_3$  and  $g$  appearing in  $\mathbf{R}$ ,  $\mathbf{M}$  and  $\mathbf{T}$  tensors

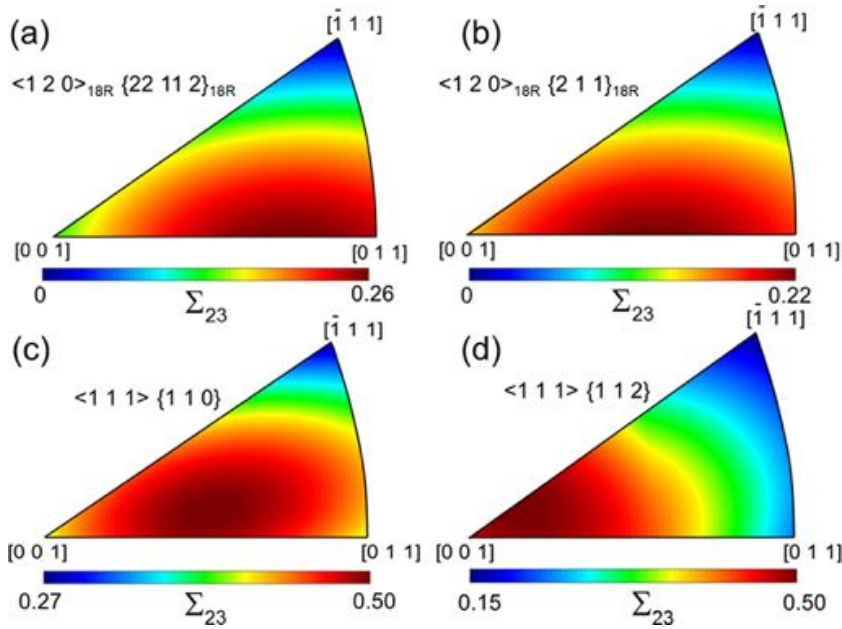


**Fig. B.2.** Stereographic projection mapping of the glide shear stresses  $\Sigma_{23}$  for the inherited slip systems of (a)  $\langle 1\ 2\ 0 \rangle_{18R} \{22\ 11\ 2\}_{18R}$  and (b)  $\langle 1\ 2\ 0 \rangle_{18R} \{2\ 1\ 1\}_{18R}$ . Similarly, (c) and (d) show the mapping of the parent  $\langle 111 \rangle \{110\}$  and  $\langle 111 \rangle \{112\}$  systems. As can be seen, the maximum resolved stresses  $\Sigma_{23}$  under unit magnitude uniaxial tensile loading are significantly different between the austenitic and the martensitic phases. Similar analogy can be also established under compression.

which are functions of the lattice parameters and the distortions measured in the stacking of the alloying atoms determined via electron microscopy (De Vos et al., 1978).

Following the values provided in Table B.2, the deformation gradient tensor  $\mathbf{F}$  (for the fundamental variant) is evaluated as:

$$\mathbf{F} = \begin{bmatrix} 0.8927 & -0.0151 & 0.1084 \\ 0.0089 & 1.0520 & -0.3169 \\ -0.0747 & -0.0619 & 1.3980 \end{bmatrix} \quad (\text{B.7})$$

Fig. B.1 illustrates the austenitic  $L2_1$  and the martensitic 18 R structures for the first 5 stacking layers based on  $\mathbf{F}$  tensor. It should be noted that the periodicity in the 18 R structure is captured at the 18th stacking layer normal to  $[0\bar{1}1]$  direction.

Construction of the  $\mathbf{F}$  tensor, allows us to establish the correspondence between any vector,  $\mathbf{m}$ , in the parent  $L2_1$  lattice structure and its inherited vector in the martensitic 18R crystal lattice,  $\mathbf{m}'$ , as follows:

$$\mathbf{m}' = \mathbf{Fm} \quad (\text{B.8})$$

Similarly, the correspondence between the parent and the inherited planes can be established by operating the deformation gradient tensor  $\mathbf{F}$  upon the cross product of the two vectors posited on the parent plane. To that end, any vector posited on a specific plane in the parent austenitic phase can be related to its post-transformation direction and plane in the martensitic phase. In particular,  $[111](\bar{1}10)$  and  $[111](\bar{1}\bar{1}2)$  glide systems in  $\beta$  phase correspond to the following set of glide systems in  $\beta'$  phase:

$$[111](\bar{1}10) \rightarrow [120]_{18R}(\bar{2}2\ 11\ \bar{2})_{18R} \quad (\text{B.9})$$

$$[111](\bar{1}\bar{1}2) \rightarrow [120]_{18R}(\bar{2}11)_{18R} \quad (\text{B.10})$$

Similar analogy can be also established for the other systems which belong to  $\langle 111 \rangle \{112\}$  or  $\langle 111 \rangle \{110\}$ .

Under uniaxial external loading, the determination of the active variant gains significance. The martensitic transformation from  $L2_1$  to 18 R structure in CuZnAl alloy consists of 24 variants (De Vos et al., 1978). Considering the correspondence of the slip systems in the austenitic and martensitic phases and the presence of the possible 24 variants; the glide stresses acting along the inherited  $[120]_{18R}(\bar{2}2\ 11\ \bar{2})_{18R}$  and  $[120]_{18R}(\bar{2}11)_{18R}$  systems vary under the uniaxial tension as shown in Fig. B.2. Comparing the resolved glide shear stress  $\Sigma_{23}$  acting on these two inherited systems and the parent  $\langle 111 \rangle \{110\}$  and  $\langle 111 \rangle \{112\}$  glide systems; it is evident that the inherited a  $\langle 111 \rangle$  superlattice dislocations to the martensitic phase are expected to exhibit a sessile behavior as the acting glide forces on the dislocations are considerably smaller in the martensitic phase. Similar analogy can be also established under uniaxial compression.

## References

- Alkan, S., Sehitoglu, H., 2017. Non-Schmid response of Fe3Al: The twin-antitwin slip asymmetry and non-glide shear stress effects. *Acta Materialia* 125, 550–566.
- Alkan, S., Wu, Y., Ojha, A., Sehitoglu, H., 2018. Transformation stress of shape memory alloy CuZnAl: Non-Schmid behavior. *Acta Materialia* 149, 220–234. doi:10.1016/j.actamat.2018.02.011.
- Alkan, S., Sehitoglu, H., 2017. Dislocation core effects on slip response of NiTi- a key to understanding shape memory. *Int. J. Plast.* 97, 126–144.
- Alkan, S., Wu, Y., Sehitoglu, H., 2017. Giant non-schmid effect in NiTi. *Extreme Mech. Lett.* 15, 38–43.
- Basinski, Z.S., Duesbery, M.S., Murty, G.S., 1981. The orientation and temperature dependence of plastic flow in potassium. *Acta Metall.* 29, 801–807.
- Chang, R., 1967. Screw dislocation core structure in body-centred cubic iron. *Philos. Mag.* 16, 1021–1029.
- Chowdhury, P., Sehitoglu, H., 2016. Significance of slip propensity determination in shape memory alloys. *Scripta Materialia* 119, 82–87.
- Chowdhury, P., Sehitoglu, H., 2017. A revisit to atomistic rationale for slip in shape memory alloys. *Prog. Mater. Sci.* 85, 1–42.
- Christian, J., 1983. Some surprising features of the plastic deformation of body-centered cubic metals and alloys. *Metall. Trans. A* 14, 1237–1256.
- Clouet, E., Caillard, D., Chaari, N., Onimus, F., Rodney, D., 2015. Dislocation locking versus easy glide in titanium and zirconium. *Nat. Mater.* 14, 931–936.
- Crawford, R., Ray, I., Cockayne, D., 1973. The weak-beam technique applied to superlattice dislocations in iron-aluminium alloys: II. fourfold dissociation in DO<sub>3</sub>-type order. *Philos. Mag.* 27, 1–7.
- Dao, M., Asaro, R.J., 1993. Non-Schmid effects and localized plastic flow in intermetallic alloys. *Mater. Sci. Eng.* 170, 143–160.
- De Vos, J.A., Etienne, Delaey, L., 1978. The crystallography of the martensitic transformation of B. C. C. into 9 R: a generalized mathematical model. *Zeitschrift für Metallkunde* 69, 438–444.
- Duesberry, M.S., 1989. The dislocation core and plasticity. In: Nabarro, F.R.N. (Ed.). In: *Dislocations in Solids*, vol. 8, pp. 67–173.
- Duesberry, M., Richardson, G., 1991. The dislocation core in crystalline materials. *Critical Rev. Solid State Mater. Sci.* 17, 1–46.
- Duesberry, M.S., Vitek, V., 1998. Plastic anisotropy in b.c.c. transition metals. *Acta Mater.* 46, 1481–1492.
- Duesberry, M.S., Vitek, V., Bowen, D.K., 1973. The effect of shear stress on the screw dislocation core structure in body-centred cubic lattices. *Proc. R. Soc. London* 332, 85.
- Duesberry, M.S., 1984. On non-glide stresses and their influence on the screw dislocation core in body-centred cubic metals. I. The Peierls stress. *Proc. R. Soc. London* 392, 145.
- Duesberry, M.S., 1984. On non-glide stresses and their influence on the screw dislocation core in body-centred cubic metals II. The core structure, proceedings of the royal society of london. series A. *Math. Phys. Sci.* 392, 175–197.
- Eshelby, J., 1949. LXXXII. Edge dislocations in anisotropic materials. *London Edinburgh Dublin Philos. Mag. J. Sci.* 40, 903–912.
- Fletcher, R., 2013. *Practical Methods of Optimization*. John Wiley & Sons.
- Foreman, A.J., Jaswon, M.A., Wood, J.K., 1951. Factors controlling dislocation widths. *Proc. Phys. Soc. Sec. A* 64, 156.
- Foreman, A.J.E., 1955. Dislocation energies in anisotropic crystals. *Acta Metall.* 3, 322–330.
- Franciosi, P., Le, L.T., Monnet, G., Kahloun, C., Chavanne, M.H., 2015. Investigation of slip system activity in iron at room temperature by SEM and AFM in-situ tensile and compression tests of iron single crystals. *Int. J. Plast.* 65, 226–249.
- Frederiksen, S.L., Jacobsen, K.W., 2003. Density functional theory studies of screw dislocation core structures in bcc metals. *Philos. Mag.* 83, 365–375.
- Gall, K., Jacobus, K., Sehitoglu, H., Maier, H.J., 1998. Stress-induced martensitic phase transformations in polycrystalline CuZnAl shape memory alloys under different stress states. *Metallurg. Mater. Trans. A* 29, 765–773.
- Gautier, E., Patoor, E., 1997. Experimental Observations for shape memory alloys and transformation induced plasticity phenomena. In: Berveiller, M., Fischer, E.D. (Eds.), *Mechanics of Solids with Phase Changes*. Springer Vienna, Vienna, pp. 69–103.
- Gröger, R., Bailey, A.G., Vitek, V., 2008. Multiscale modeling of plastic deformation of molybdenum and tungsten: I. Atomistic simulation of the core structure and glide of 1/2{111} screw dislocations at 0K. *Acta Mater.* 56, 5401–5411.
- Gröger, R., Racherla, V., Bassani, J.L., Vitek, V., 2008. Multiscale modeling of plastic deformation of molybdenum and tungsten: II. Yield criterion for single crystals based on atomistic studies of glide of screw dislocations. *Acta Mater.* 56, 5412–5425.
- Hill, R., 1998. *The Mathematical Theory of Plasticity*. Oxford university press.
- Hirth, J., Lothe, J., 1968. *Theory of Dislocations*. McGraw Hill Book Company.
- Hu, Y.-F., Deng, W., Hao, W.E.N.B., Yue, L., Huang, L., Huang, Y.-Y., Xiong, L.-Y., 2006. Microdefects and electron densities in NiTi shape memory alloys studied by positron annihilation. *Trans. Nonferrous Metals Soc. China* 16, 1259–1262.
- Jara, D.R., Esnouf, C., Guénin, G., 1985. A quantitative study of stable dislocations in the  $\beta$ 1-phase of Cu-Zn-Al alloys. *Physica Status Solidi (a)* 87, 187–197.
- Kresse, G., Furthmüller, J., 1996. Efficient iterative schemes for ab initio total-energy calculations using a plane-wave basis set. *Phys. Rev. B* 54, 11169–11186.
- Kresse, G., Hafner, J., 1993. Ab initio. *Phys. Rev. B* 48, 13115–13118.
- Kroupa, F., Lejček, L., 1972. Splitting of dislocations in the Peierls-Nabarro model. *Czech. J. Phys. B* 22, 813–825.
- Kroupa, F., Vitek, V., 1967. Slip and the conception of splitting of dislocations in b.c.c. metals. *Can. J. Phys.* 45, 945–971.
- Lejček, L., Kroupa, F., 1981. The effect of shear stress on the screw dislocation core in bcc metals. *Czechoslovak J. Phys.* 31, 719–723.
- Lejček, L., 1973. On minimum of energy in the Peierls-Nabarro dislocation model. *Czech. J. Phys. B* 23, 176–178.
- Lejček, L., 1979. Method of an approximate solution of the Peierls-Nabarro equations for non-planar screw dislocation cores. *Czech. J. Phys. B* 29, 196–202.
- Lim, H., Weinberger, C.R., Battaile, C.C., Buchheit, T.E., 2013. Application of generalized non-Schmid yield law to low-temperature plasticity in bcc transition metals. *Model. Simul. Mater. Sci. Eng.* 21, 045015.
- Lin, Y.-S., Cak, M., Paidar, V., Vitek, V., 2012. Why is the slip direction different in different B2 alloys? *Acta Materialia* 60, 881–888.
- Lothe, J.P.H.J., 1982. *Theory of Dislocations*, second ed. Krieger Pub. Co.
- Lothe, J.P.H.J., 1992. *Theory of Dislocations*, second ed. Krieger Pub. Co.
- Lovey, F.C., Torra, V., 1999. Shape memory in Cu-based alloys: phenomenological behavior at the mesoscale level and interaction of martensitic transformation with structural defects in Cu-Zn-Al. *Prog. Mater. Sci.* 44, 189–289.
- Marichal, C., Van Swygenhoven, H., Van Petegem, S., Borca, C., 2013. {110} Slip with {112} slip traces in bcc Tungsten. *Sci. Rep.* 3, 2547.
- Otsuka, K., Wayman, C.M. (Eds.), 1998. *Shape Memory Materials*. Cambridge University Press, Cambridge.
- Patra, A., Zhu, T., McDowell, D.L., 2014. Constitutive equations for modeling non-Schmid effects in single crystal bcc-Fe at low and ambient temperatures. *Int. J. Plast.* 59, 1–14.
- Polyanin, A.D., Manzhirov, A.V., 2008. *Handbook of Integral Equations*. CRC press.
- Qin, Q., Bassani, J.L., 1992. Non-schmid yield behavior in single crystals. *J. Mech. Phys. Solids* 40, 813–833.
- Romero, R., Ahlers, M., 1989. The influence of  $\beta$ -phase plastic deformation on the martensitic transformation in Cu-Zn-Al single crystals. *Philos. Mag. A* 59, 1103–1112.
- Romero, R., Lovey, F., Ahlers, M., 1988. Plasticity in  $\beta$  phase Cu-Zn-Al alloys. *Philos. Mag. A* 58, 881–903.
- Sade, M., Uribarri, A., Lovey, F., 1987. An electron-microscopy study of dislocation structures in fatigued Cu-Zn-Al shape-memory alloys. *Philos. Mag. A* 55, 445–461.
- Sade, M., Damiani, C., Gastien, R., Lovey, F.C., Malarría, J., Yawny, A., 2007. Fatigue and martensitic transitions in Cu-Zn-Al and Cu-Al-Ni single crystals: mechanical behaviour, defects and diffusive phenomena. *Smart Mater. Struct.* 16, S126.
- Schmid, E., Boas, W., 1950. *Plasticity of Crystals*. A. Hughes and Co., London.
- Šesták, B., Zárubová, N., 1965. Asymmetry of slip in Fe-Si alloy single crystals. *Phys. Status Solidi (b)* 10, 239–250.
- Sherwood, P.J., Guiu, F., Kim, H.C., Pratt, P.L., 1967. Plastic anisotropy of Tantalum, Niobium, and Molybdenum. *Can. J. Phys.* 45, 1075–1089.
- Steeds, J.W., 1973. *Introduction to Anisotropic Elasticity Theory of Dislocations*. Clarendon Press.

- Sutou, Y., Omori, T., Kainuma, R., Ishida, K., 2008. Ductile Cu–Al–Mn based shape memory alloys: general properties and applications. *Mater. Sci. Tech.* 24, 896–901.
- Suzuki, H., 1968. Motion of Dislocations in Body-Centered Cubic Crystals. *Dislocation Dynamics* McGraw-Hill USA, pp. 679–700.
- Tadmor, E.B., Miller, R.E., 2011. *Modeling materials - continuum, atomistic and multiscale technique*. Cambridge University Press.
- Taylor, G.I., 1928. The deformation of crystals of  $\beta$ -Brass. *Proc. R. Soc. London. Series A* 118, 1–24.
- Taylor, G., 1992. Thermally-activated deformation of BCC metals and alloys. *Prog. Mater. Sci.* 36, 29–61.
- Vitek, V., Kroupa, F., 1969. Generalized splitting of dislocations. *Philos. Mag.* 19, 265–284.
- Vitek, V., Perrin, R.C., Bowen, D.K., 1970. The core structure of  $\frac{1}{2}(111)$  screw dislocations in b.c.c. crystals. *Philos. Mag.* 21, 1049–1073.
- Verlinden, B., Suzuki, T., Delaey, L., Guenin, G., 1984. Third order elastic constants of  $\beta$  Cu-Zn-Al as a function of the temperature. *Scripta Metall.* 18, 975–979.
- Vitek, V., Paidar, V., 2011. Nonplanar dislocation cores: a ubiquitous phenomenon affecting mechanical properties of crystalline materials. In: Hirth, J.P. (Ed.), *Dislocations in Solids*. Elsevier B.V., Chapter 87.
- Vitek, V., Lejček, L., Bowen, D., 1972. On the factors controlling the structure of dislocation cores in bcc crystals. In: *Interatomic Potentials and Simulation of Lattice Defects*. Springer, pp. 493–508.
- Vitek, V., 1968. Intrinsic stacking faults in body-centred cubic crystals. *Philos. Mag.* 18, 773.
- Vitek, V., 1974. Theory of the core structures of dislocations in body-centred-cubic metals. *Crystal Lattice Defects* 5, 1–34.
- Vitek, V., 1985. Effect of dislocation core structure on the plastic properties of metallic materials. In: *Fiftieth Anniversary of the Concept of Dislocation in Crystals*. The Institute of Metals, London, pp. 30–50.
- Wang, J., Sehitoglu, H., 2014. Dislocation slip and twinning in Ni-based L12 type alloys. *Intermetallics* 52, 20–31.
- Wang, G., Strachan, A., Cagin, T., Goddard, W.A., 2001. Molecular dynamics simulations of  $\frac{1}{2} a(111)$  screw dislocation in Ta. *Mater. Sci. Eng. A* 309, 133–137.
- Wayman, C.M., 1980. Some applications of shape-memory alloys. *JOM* 32, 129–137.
- Wechsler, M.S., Lieberman, D.S., Read, T.A., 1953. On theory of formation of martensite. *J. Metals* 5, 1503–1515.
- Woodward, C., Rao, S.I., 2001. Ab-initio simulation of isolated screw dislocations in bcc Mo and Ta. *Philos. Mag. A* 81, 1305–1316.
- Wu, Y., Ojha, A., Patriarca, L., Sehitoglu, H., 2015. Fatigue crack growth fundamentals in shape memory alloys. *Shape Memory Superelast.* 1, 18–40.
- Wu, Y., Ertekin, E., Sehitoglu, H., 2017. Elastocaloric cooling capacity of shape memory alloys – Role of deformation temperatures, mechanical cycling, stress hysteresis and inhomogeneity of transformation. *Acta Mater.* 135, 158–176.
- Wu, M.H., 1990. Cu-based shape memory alloys A2 - Duerig, T W. In: Melton, K.N., Stöckel, D., Wayman, C.M. (Eds.), *Engineering Aspects of Shape Memory Alloys*. Butterworth-Heinemann, pp. 69–88.
- Yamaguchi, M., Umakoshi, Y., 1983. Dislocations in b.c.c. metals and ordered alloys and compounds with b.c.c.-based ordered structures. In: Paidar, V., Lejček, L. (Eds.), *The Structure and Properties of Crystal Defects*. Elsevier, Czechoslovakia.